Reflective Metasurfaces with Multiple Elastic Mode Conversions for Broadband Underwater Sound Absorption

Hao-Wen Dong,[1,2] Sheng-Dong Zhao,[3] Mourad Oudich,[4,5,*] Chen Shen,[6] Chuanzeng Zhang,[7] Li Cheng,[2,†] Yue-Sheng Wang,[8,‡] and Daining Fang[1,§]

[1] *Institute of Advanced Structure Technology, Beijing Institute of Technology, Beijing, 100081, China*
[2] *Department of Mechanical Engineering, The Hong Kong Polytechnic University, Kowloon 999077, Hong Kong*
[3] *School of Mathematics and Statistics, Qingdao University, Qingdao 266071, China*
[4] *Graduate Program in Acoustics, The Pennsylvania State University, University Park, Pennsylvania 16802, USA*
[5] *Université de Lorraine, CNRS, Institut Jean Lamour, F-54000 Nancy, France*
[6] *Department of Mechanical Engineering, Rowan University, Glassboro, New Jersey 08028, USA*
[7] *Department of Civil Engineering, University of Siegen, D-57068 Siegen, Germany*
[8] *Department of Mechanics, School of Mechanical Engineering, Tianjin University, Tianjin 300350, China*

(Received 16 December 2021; accepted 7 March 2022; published 7 April 2022)

Unlike their electromagnetic and acoustic counterparts, elastic waves involve different wave modes. The interplay and the coupling among them increase the complexity of the problem while also offering a larger space for wave manipulation. Elastic bulk wave conversion in an elastic metamaterial has recently shown great promise in medical ultrasound and nondestructive testing. Unlike the transmission-type conversion, however, reflective elastic mode conversion has been explored less in terms of analysis and design, despite the enormous possibilities that it might offer for energy trapping and dissipation. In this work, we develop a theoretical framework for constructing elastic anisotropic metasurfaces that can enable reflective longitudinal-to-transverse (L-to-T) and transverse-to-longitudinal (T-to-L) wave conversions. We capitalize on the mechanism of multiple reflective mode conversion to achieve broadband, subwavelength, and near perfect sound absorption in the underwater environment. The reflective scattering properties of the metasurfaces are systematically exploited for incident longitudinal or transverse waves. The conversion mechanism is rooted in reflective Fabry-Perot (FP) resonance, whose occurrence conditions and features are predicted for prescribed effective parameters of the metasurface. We then establish an inverse-design framework for conceiving an underwater coating system formed by a viscoelastic rubber layer and the metasurface. A series of metasurfaces allowing for customized mode conversions are realized for delivering broadband low-frequency and high-efficiency underwater sound absorption. Specifically, an ultrathin rubber-metasurface layer in which the metasurface with a thickness of approximately $\lambda/70$ can lead to nearly 100% sound absorption. Furthermore, we demonstrate that a persistently high absorption (over 80%) can be obtained in a rather robust manner within a wide range of wave incidence angle from $-60°$ to $60°$. More importantly, high-efficiency acoustic absorption exceeding 75% can be readily achieved through multiple mode conversions within the ultrabroadband range featuring a relative bandwidth of 119%. We reveal the combined FP resonance mechanism of underwater sound absorption, i.e., the FP resonance of the metaconverter, which determines the L-to-T and T-to-L conversion ratio, and the FP resonance of the rubber-metasurface layers, which enhances the wave attenuation inside the rubber. The proposed reflective multiple mode-conversion mechanism and metasurface design methodology open a route towards a class of elastic-wave-based devices with promising potential for underwater applications.

DOI: 10.1103/PhysRevApplied.17.044013

I. INTRODUCTION

Over the past decade, elastic metamaterials [1–9] have been proposed with diverse combinations of effective constitutive parameters to produce new physical phenomena, which entail numerous functionalities and applications for elastic waves. Owing to the designability of structures at both macro- and microscales, judiciously designed elastic metamaterials allow for the selective control of wave propagation and polarization in a solid, namely ensuring the propagation of a particular elastic wave mode while preventing the transmission of other wave components. The idea has been exploited in the open

*mourad.oudich@univ-lorraine.fr
†li.cheng@polyu.edu.hk
‡yswang@tju.edu.cn
§fangdn@bit.edu.cn

literature. For example, when effective single negativity is combined with multipolar resonances, metamaterials can carry pure longitudinal (L) waves with a hyperbolic feature [8]. For multiple-phase [4] or single-phase [8] metamaterials that simultaneously have negative mass density, negative longitudinal modulus, and positive shear modulus, pure longitudinal wave propagation can be realized within a low-frequency range while transverse (T) waves are completely prohibited. Conversely, if the metamaterials have an effective negative mass density, negative shear modulus, but positive longitudinal modulus [3,8], only the pure transverse wave can propagate within the metamaterials [3]. By designing microstructures with the pentamode feature, it is feasible to construct pentamode metamaterials, which only support broadband pure longitudinal waves as well [9]. In addition to the control of pure longitudinal or transverse waves, it is also possible to subtly manipulate the single polarizations of other elastic waves in metamaterials [10–13]. When the anisotropic mass density is combined with kirigami plates, hyperlensing of pure flexural waves can be achieved [10]. Similarly, a double-negative double-sided pillared metamaterial can only support the propagation of a symmetric Lamb wave with the forbidden nature of an antisymmetric Lamb wave [11]. Analogous to the bound state in the continuum, the elastic metasurface can cause low-frequency perfect conversion between flexural and longitudinal waves [12]. Furthermore, the subwavelength resonators and suitable Rayleigh wave interaction can lead to slow Rayleigh waves through seismic metamaterials [13,14]. As basic wave forms, pure longitudinal or transverse wave manipulation is essential for nondestructive testing, medical ultrasound, and even underwater sound applications.

In recent years, elastic metamaterials allowing for longitudinal-to-transverse (L-to-T) wave conversion have attracted increasing attention from multidisciplinary scientists because of the potential applications they may enable, ranging from vibration insulation, nondestructive evaluation, and ultrasound sensing to structural health monitoring [3,15–17]. Different effective features can give rise to mode conversion in the metamaterials. Transmodal anisotropic mode-coupling metamaterials based on Fabry-Perot (FP) resonance can realize high-efficiency and even perfect L-to-T conversion [16,18]. In addition to anisotropic metamaterials, double-negative ones offer another option for L-to-T wave conversion. Typical L-to-T conversion phenomena can be induced at the interface between a background medium and metamaterials with simultaneous negative density and longitudinal modulus [15]. Conversely, double-negative metamaterials with simultaneous negative density and shear modulus can transform the incident transverse wave into the reflected longitudinal wave at the interface [3]. Based on the generalized Snell's law, elastic metasurfaces with a large phase gradient can accomplish broad-angle mode conversion between L and T waves [17].

So far, most studies have focused on the transmissive L-to-T conversion [3,15–18] in elastic metamaterials. However, the reflective L-to-T or T-to-L conversion has not been well explored. The potential benefit of elaborately constructed reflective mode conversion for enhancing the acoustic absorption and even perfect absorption is yet to be exploited. The problem is particularly relevant for underwater sound absorption of metamaterials, which has close ties with the control of longitudinal and transverse waves, including mode conversion, scattering features, and propagation characteristics. Existing underwater absorber designs are mostly based on a viscoelastic coating layer containing either air-filled cavities [19,20], high-density rigid spheres [21,22], or softly coated resonant units [23]. These structures can either perform at high frequencies (in the megahertz range) with nearly perfect absorption for the case of air-filled cavities, or operate at low frequencies (below 10 kHz) for the case of high-density spheres where resonance is used to enhance the viscoelastic loss. Unfortunately, the resonance mechanism limits the absorption efficacy to narrow frequency bands, and the metamaterial is usually bulky to cope with the large wavelength of underwater sound. To solve this challenge, alternative solid structures with manipulated propagation characteristics for elastic waves are much needed.

The ultimate goal of this paper is to achieve perfect and even broadband underwater sound absorption utilizing the reflective mode-conversion mechanism of the rubber-metasurface system. Meanwhile, the underlying physics governing the phenomena is also analyzed. More specifically, we develop a scattering model of the elastic anisotropic metasurface and propose an inverse-design methodology with customized mode couplings to achieve reflective L-to-T and T-to-L conversion. Based on the scattering model, we systematically analyze the dominant role of the dynamic effective parameters on the reflection and polarization of longitudinal and transverse waves. In particular, the condition for maximal reflective conversion based on the phase difference between the quasilongitudinal (QL) and quasitransverse (QT) modes is discovered through the scattering model. Subsequently, the reflective mode-conversion FP resonance frequencies for arbitrary effective parameters are analytically predicted. To validate the scattering theory and wave behavior, we establish a unified inverse-design framework to design anisotropic elastic metasurfaces exhibiting arbitrarily prescribed effective parameters. A series of ultrathin anisotropic metasurfaces is customized and analyzed to clarify the beneficial asymmetric network topology for the reflective mode conversion. Furthermore, extensive underwater demonstrations are conducted to verify the wave functionality of metasurfaces with distinct anisotropy

and mode coupling. The low-frequency high-efficiency absorption is showcased through a coating layer comprising viscoelastic rubber and a metasurface. Specifically, taking advantage of the impedance matching with water and the high dissipation effect on T waves of the rubber, a rubber-metasurface bilayer with a thickness of approximately $\lambda/70$ is shown to achieve low-frequency perfect sound absorption. The conceived metasurface can enable a high sound absorption of over 80% for a wide range of incident wave angles, $-60°$ to $60°$. Meanwhile, the metasurface can deliver high-efficiency absorption exceeding 75% within an ultrabroadband range with a relative bandwidth of 119%. Regarding methodology, the proposed topology optimization model of anisotropic elastic metasurfaces can accommodate arbitrary mode coupling on demand. In the rubber-metasurface system, we discover the combined mode-conversion FP resonance and generalized FP resonance for generating elaborative scattering properties. Overall, we develop a family of elastic metamaterials capable of reflective mode conversion for the ultimate benefit of controlling elastic wave energy. The approach can achieve effective underwater sound absorption in deep subwavelength scales. Such a mechanism has neither been explored nor used for underwater absorption applications.

Unlike the transmissive type [16], reflective L-to-T or T-to-L conversion requires scattering control and specific boundary conditions for energy dissipation through a solid medium. Additionally, existing studies have only dealt with the design of metamaterials with single-way transmissive mode conversion, however, multiple mode conversion exists in the reflective mode-conversion system. More importantly, reflective mode conversion may be of greater application value, in view of vibration isolation, elastic wave absorption, nondestructive testing, achieving underwater sound absorption, ultrasound transducers, and even integrated absorption-insulation functionalities. Our study significantly differs from the existing works on mode conversion in several aspects: (a) Different wave functionality. Our study focuses on reflective elastic wave control (involving multiple reflections within the rubber-metasurface bilayer) instead of the previous transmissive one. For example, the work of Kweun *et al.* [16] is essentially single-way transmissive. Although the possibility of a reflective conversion was mentioned in their supplementary material, a realistic design of reflective-type converters was not realized. (b) Different mode-conversion mechanism. Previously reported mode conversion is essentially single-way transmissive. We here demonstrate that the rubber-metasurface system can possess multiple L-to-T and T-to-L conversions when the mode conversion ratio is relatively large. (c) Different underwater sound absorption mechanism. Unlike the traditional locally resonant structures, the present subwavelength underwater absorption is achieved through reflective mode conversion, which has never been studied and reported. Our approach enables broadband sound absorption, which can hardly be attained by classical resonant systems.

This paper is organized as follows. Section II establishes an elastic wave theory of anisotropic metasurfaces with reflective mode conversion. Based on the scattering model, effects of the effective parameters on the reflection of longitudinal and transverse waves are systematically investigated. The conditions and reflective mode-conversion FP resonance frequencies are derived as well. Section III firstly describes the dynamic effective medium theory of anisotropic elastic metasurfaces. Subsequently, a unified inverse-design model of metasurfaces is established for obtaining arbitrarily prescribed effective parameters. Then, some representative inverse-designed metasurfaces are analyzed and discussed. In Sec. IV, simulations are carried out to verify the mode-conversion properties in relation to underwater absorption. Section V summarizes the main contributions of the study and gives the outlook of elastic reflective metasurfaces. The present study provides a complete reflective mode-conversion design methodology for elastic metamaterials, which opens a paradigm towards building customized anisotropic mode-coupling elastic solids for elastic wave energy dissipation and underwater low-frequency sound absorption with high efficiency.

II. THEORY OF REFLECTIVE METASURFACES WITH MODE CONVERSION

Underwater low-frequency sound absorption by solids is of vital importance in engineering. In fact, the manipulation of elastic waves in the solid medium under strong fluid-solid coupling conditions lies at the core of scientific problems. To achieve underwater low-frequency perfect acoustic or sound absorption, we propose a specific coating layer composed of a viscoelastic rubber layer and an anisotropic elastic metamaterial as shown in Fig. 1(a). Under incident acoustic waves, the coating is expected to generate reflective L-to-T wave conversion for high-efficiency low-frequency absorption, and so be used as a reflective metasurface for underwater sound absorption. The bilayer system [Fig. 1(a)] comprises a viscoelastic layer (polydimethylsiloxane or rubber) and a solid metasurface. As waves in water are exclusively longitudinal, the incident wave will first excite L waves in the polydimethylsiloxane layer, then in the metasurface, where L waves will be converted to T waves through FP resonance. Unable to propagate in water, the resultant T waves will be trapped in the viscoelastic and metasurface layers, giving rise to multiple reflections and therefore strong losses over a short distance. Since T waves have smaller wavelengths than L waves, their decay distance is smaller, which reduces the coating thickness required.

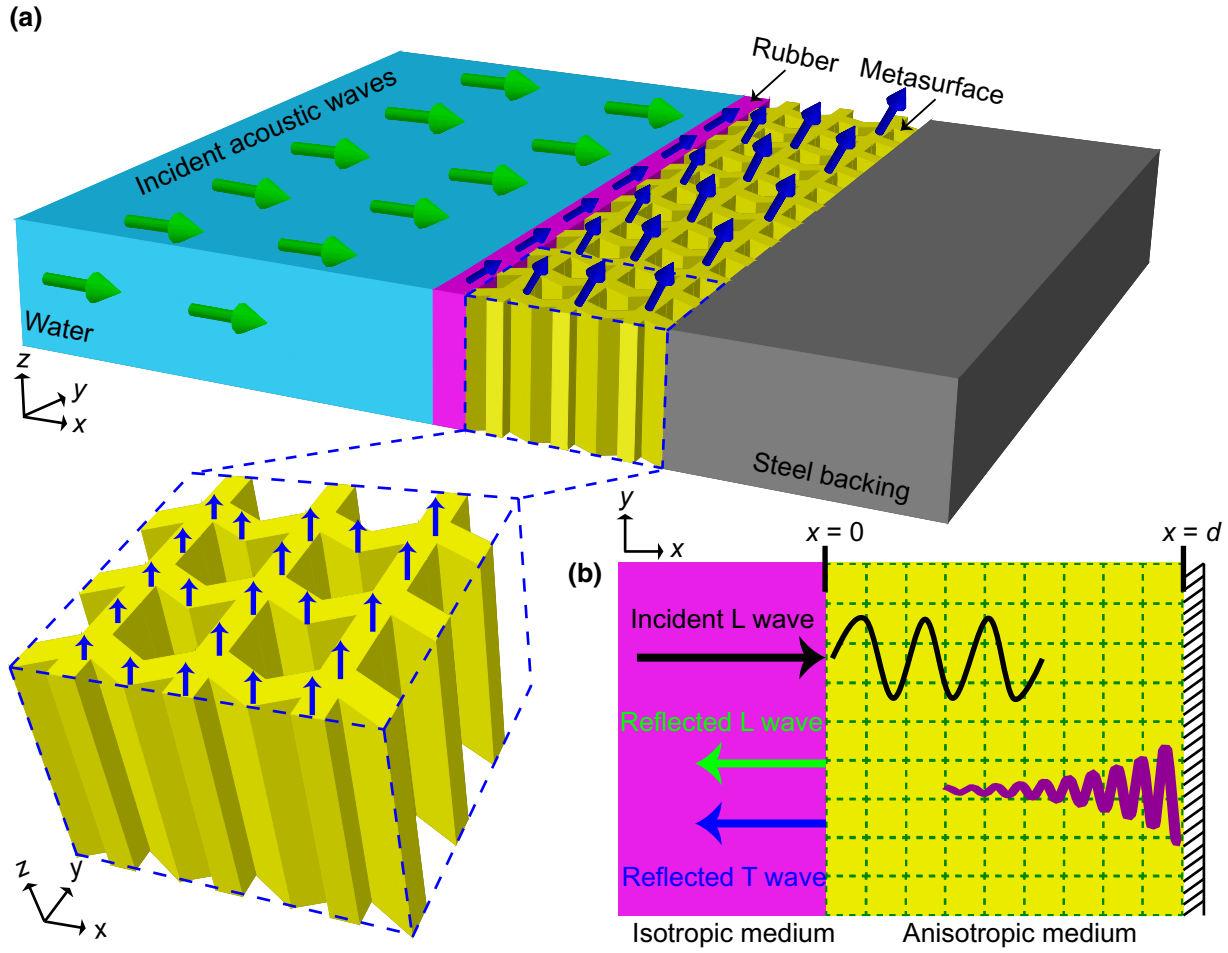

FIG. 1. Schematic of an elastic metasurface for underwater sound absorption. (a) The underwater coating, composed of a viscoelastic layer (rubber), whose acoustic impedance matches with the water, and an elastic metasurface, fixed on a steel backing. Arrows represent the directions of polarization. The size of an arrow loosely denotes the particle vibration magnitude. (b) Model of converting the incident L waves into the reflected L and T waves at the interface between the isotropic and anisotropic media, which consist of periodic anisotropic elastic microstructures. The right-hand end of the model is fixed to achieve the boundary condition between the steel backing and metasurface shown in (a).

To realize the reflective mode conversion, we first consider the corresponding solid-solid model built in Fig. 1(b) where the isotropic and anisotropic solid media are interconnected. In particular, the solid-solid model is fixed on the rigid body to be like a practical clamped boundary. Given longitudinal wave propagation along the x direction, the wave motion inside the metamaterial obviously depends on the parameters of the isotropic and anisotropic solids. Upon L wave incidence, the waves with coupled L and T modes will propagate in the anisotropic solid. Then the right-hand fixed boundary will reflect the waves back into the solids, thus producing reflected L and T waves from the solid-solid interface.

Note that the present model aims at the challenging problem of achieving high-efficiency underwater sound absorption. The fluid-solid coupling and the unavoidable loss in the underwater environment entail rich yet complex physical phenomena, whose comprehension is challenging in terms of modeling, analysis, and design. To achieve high sound absorption efficiency, perfect impedance matching has to be guaranteed at the two interfaces of the model, i.e., the water-rubber interface and the rubber-metamaterial interface. Therefore, the effective impedance of the rubber is set to be the same as that of the water. Meanwhile, both the mass density and elastic longitudinal modulus C_{11} of the metamaterial need to be the same as those of the rubber to neutralize reflections at the two interfaces. The reflective T waves at the interface are induced by the anisotropic metamaterial. These salient features, as well as the adoption of the plane strain condition instead of the plane stress condition, differ from the existing work on similar topics [16]. These will be discussed in detail in the following sections.

A. Scattering model for the reflective elastic anisotropic metasurfaces

The wave motion in Fig. 1(b) is described by a scattering model. For a general anisotropic elastic medium, the equations of motion and elastic constitutive equations are given by

$$\begin{aligned} \nabla \cdot \boldsymbol{\sigma} &= \rho \ddot{\mathbf{u}} \\ \boldsymbol{\sigma} &= \boldsymbol{C} : \nabla \mathbf{u} \end{aligned}, \tag{1}$$

where ∇ is the Laplace operator, $\boldsymbol{\sigma}$ is the second-order stress tensor, ρ is the mass density, ":" denotes the double dot product, $\mathbf{C}$ is the fourth-order elasticity tensor, and $\mathbf{u}$ represents the displacement vectors.

To characterize the wave propagation within the elastic anisotropic metamaterial, the scattering theory and model are systematically built for the solid system containing the rubber and the metasurface. Considering normal incident time-harmonic elastic plane waves propagating along the x direction, as shown in Fig. 1(b), the displacement field $\mathbf{u} = (u_x, u_y)$ in the background isotropic medium (rubber) is defined as

$$\begin{aligned} u_x &= u^i_{x,0} e^{-ik_{\mathrm{L}}x} + u^r_{x,0} e^{ik_{\mathrm{L}}x} \\ u_y &= u^i_{y,0} e^{-ik_{\mathrm{T}}x} + u^r_{y,0} e^{ik_{\mathrm{T}}x} \end{aligned}, \tag{2}$$

where u_x and u_y are the displacements along x and y directions, respectively; $u^i_{x,0}$ and $u^i_{y,0}$ represent the incident displacement amplitudes; $u^r_{x,0}$ and $u^r_{y,0}$ express the reflected displacement amplitudes; $k_{\mathrm{L}} = \omega/\sqrt{C^0_{11}/\rho_0}$ and $k_{\mathrm{T}} = \omega/\sqrt{C^0_{66}/\rho_0}$ are the wave numbers of longitudinal and transverse waves; and ω is the angular frequency. Throughout the paper, the time-harmonic term $e^{i\omega t}$ is omitted for the sake of brevity.

The constitutive relation in the background isotropic medium is written as

$$\begin{Bmatrix} \sigma_{xx} \\ \sigma_{yy} \\ \sigma_{xy} \end{Bmatrix} = \begin{bmatrix} C^0_{11} & C^0_{12} & 0 \\ C^0_{12} & C^0_{11} & 0 \\ 0 & 0 & C^0_{66} \end{bmatrix} \begin{Bmatrix} \frac{\partial u_x}{\partial x} \\ \frac{\partial u_y}{\partial y} \\ \frac{\partial u_x}{\partial y} + \frac{\partial u_y}{\partial x} \end{Bmatrix}, \tag{3}$$

where C^0_{11} and C^0_{12} represent the elastic longitudinal and coupling moduli of the background solid, and the shear modulus is $C^0_{66} = (C^0_{11} - C^0_{12})/2$.

Considering the L wave along the x direction, Eq. (3) for the one-dimensional case can be simplified as

$$\begin{aligned} \sigma_{xx} &= C^0_{11} \frac{\partial u_x}{\partial x} \\ \sigma_{xy} &= C^0_{66} \frac{\partial u_y}{\partial x} \end{aligned}. \tag{4}$$

For the anisotropic medium (metasurface) shown in Fig. 1(b), the displacement field $\mathbf{u}$ is expressed as

$$\begin{aligned} u_x &= P_x(Ae^{-i\alpha x} + Be^{i\alpha x}) + Q_x(Ce^{-i\beta x} + De^{i\beta x}) \\ u_y &= P_y(Ae^{-i\alpha x} + Be^{i\alpha x}) + Q_y(Ce^{-i\beta x} + De^{i\beta x}) \end{aligned}, \tag{5}$$

where A, B, C, and D denote the displacement amplitudes of the QL and QT modes, respectively; P_x, P_y, Q_x, Q_y are the corresponding polarization components.

Furthermore, for the anisotropic medium, the constitutive equation is written as

$$\begin{Bmatrix} \sigma_{xx} \\ \sigma_{yy} \\ \sigma_{xy} \end{Bmatrix} = \begin{bmatrix} C_{11} & C_{12} & C_{16} \\ C_{12} & C_{22} & C_{26} \\ C_{16} & C_{26} & C_{66} \end{bmatrix} \begin{Bmatrix} \frac{\partial u_x}{\partial x} \\ \frac{\partial u_y}{\partial y} \\ \frac{\partial u_x}{\partial y} + \frac{\partial u_y}{\partial x} \end{Bmatrix}. \tag{6}$$

The corresponding Christoffel's equation for the plane time-harmonic bulk waves is given by

$$\begin{bmatrix} C_{11}k^2 - \rho\omega^2 & C_{16}k^2 \\ C_{16}k^2 & C_{66}k^2 - \rho\omega^2 \end{bmatrix} \begin{Bmatrix} u_x \\ u_y \end{Bmatrix} = 0, \tag{7}$$

where k is the wave number.

When deriving the nontrivial solution of Eq. (6), with the condition of $C^2_{16} < C_{11}C_{66}$, the wave numbers α and β of the QL and QT modes are respectively determined by

$$\begin{aligned} \alpha &= \omega \sqrt{\frac{\rho_M \left[C_{11} + C_{66} - \sqrt{(C_{11} - C_{66})^2 + 4C^2_{16}} \right]}{2(C_{11}C_{66} - C^2_{16})}} \\ \beta &= \omega \sqrt{\frac{\rho_M \left[C_{11} + C_{66} + \sqrt{(C_{11} - C_{66})^2 + 4C^2_{16}} \right]}{2(C_{11}C_{66} - C^2_{16})}} \end{aligned}, \tag{8}$$

where ρ_M represents the mass density of the anisotropic metamaterial.

The corresponding wave polarization vectors (P_x, P_y) and (Q_x, Q_y) for the QL and QT modes are respectively given by

$$\begin{aligned} P_x &= \frac{X_{\mathrm{QL}}}{\sqrt{1 + |X_{\mathrm{QL}}|^2}} \\ P_y &= \frac{1}{\sqrt{1 + |X_{\mathrm{QL}}|^2}} \\ Q_x &= \frac{X_{\mathrm{QT}}}{\sqrt{1 + |X_{\mathrm{QT}}|^2}} \\ Q_y &= \frac{1}{\sqrt{1 + |X_{\mathrm{QT}}|^2}} \end{aligned}, \tag{9}$$

where X_{QL} and X_{QT} are defined as

$$\begin{aligned} X_{\mathrm{QL}} &= -\frac{C_{16}\alpha^2}{C_{11}\alpha^2 - \rho_M\omega^2} \\ X_{\mathrm{QT}} &= -\frac{C_{66}\beta^2 - \rho_M\omega^2}{C_{16}\beta^2} \end{aligned}. \tag{10}$$

Similarly, only the normally incident L wave propagating along the x direction is considered. As a result, the above Hooke's law for the one-dimensional regime can be reduced to

$$\begin{aligned} \sigma_{xx} &= C_{11}\frac{\partial u_x}{\partial x} + C_{16}\frac{\partial u_y}{\partial x} \\ \sigma_{xy} &= C_{16}\frac{\partial u_x}{\partial x} + C_{66}\frac{\partial u_y}{\partial x} \end{aligned}, \tag{11}$$

where σ_{xx} and σ_{xy} only depend on C_{11}, C_{16}, and C_{66} of the anisotropic metamaterial.

According to the continuity condition of the displacement field at $x=0$ in Fig. 1(b), Eqs. (2) and (5) yield

$$\begin{aligned} u^i_{x,0} + u^r_{x,0} &= P_x(A+B) + Q_x(C+D) \\ u^i_{y,0} + u^r_{y,0} &= P_y(A+B) + Q_y(C+D) \end{aligned}. \tag{12}$$

Similarly, from the continuity condition of the stress components σ_{xx} and σ_{xy} at $x=0$, Eqs. (4) and (11) lead to

$$\begin{aligned} k_{\mathrm{L}}C^0_{11}(u^i_{x,0} - u^r_{x,0}) &= \alpha(A-B)(C_{11}P_x + C_{16}P_y) \\ &\quad + \beta(C-D)(C_{11}Q_x + C_{16}Q_y), \end{aligned} \tag{13}$$

$$\begin{aligned} k_{\mathrm{T}}C^0_{66}(u^i_{y,0} - u^r_{y,0}) &= \alpha(A-B)(C_{16}P_x + C_{66}P_y) \\ &\quad + \beta(C-D)(C_{16}Q_x + C_{66}Q_y). \end{aligned} \tag{14}$$

Considering the fixed boundary condition at $x=d$ in Fig. 1(b) [$\mathbf{u}(x=d)=\mathbf{0}$], one has from Eq. (5)

$$\begin{aligned} P_x(Ae^{-i\alpha d} + Be^{i\alpha d}) + Q_x(Ce^{-i\beta d} + De^{i\beta d}) &= 0 \\ P_y(Ae^{-i\alpha d} + Be^{i\alpha d}) + Q_y(Ce^{-i\beta d} + De^{i\beta d}) &= 0 \end{aligned}. \tag{15}$$

The determinant of the system matrix of Eq. (15) can be obtained as

$$P_xQ_y - P_yQ_x = \frac{(C_{11}\alpha^2 - \rho_{\mathrm{M}}\omega^2)(C_{66}\beta^2 - \rho_{\mathrm{M}}\omega^2) - C^2_{16}\alpha^2\beta^2}{C_{16}\beta^2(C_{11}\alpha^2 - \rho_{\mathrm{M}}\omega^2)}. \tag{16}$$

After some mathematical manipulations, Eq. (16) can be rewritten as

$$P_xQ_y - P_yQ_x = \frac{-\sqrt{(C_{11}-C_{66})^2 + 4C^2_{16}}\left[\sqrt{(C_{11}-C_{66})^2 + 4C^2_{16}} - (C_{11}-C_{66})\right]}{2C_{16}\beta^2(C_{11}\alpha^2 - \rho_M\omega^2)(C_{11}C_{66} - C^2_{16})}, \tag{17}$$

which should be nonzero if C_{16} is not equal to 0.

Consequently, the expressions for B and D can be written as

$$B = -Ae^{-2i\alpha d}, \tag{18}$$

$$D = -Ce^{-2i\beta d}. \tag{19}$$

Substituting Eqs. (18) and (19) into Eqs. (12)–(14) gives

$$u^i_{x,0} + u^r_{x,0} = AP_x(1 - e^{-2i\alpha d}) + CQ_x(1 - e^{-2i\beta d}), \tag{20}$$

$$u^i_{y,0} + u^r_{y,0} = AP_y(1 - e^{-2i\alpha d}) + CQ_y(1 - e^{-2i\beta d}), \tag{21}$$

$$\begin{aligned} u^i_{x,0} - u^r_{x,0} &= \frac{\alpha A}{k_{\mathrm{L}}C^0_{11}}(1 + e^{-2i\alpha d})(C_{11}P_x + C_{16}P_y) \\ &\quad + \frac{\beta C}{k_{\mathrm{L}}C^0_{11}}(1 + e^{-2i\beta d})(C_{11}Q_x + C_{16}Q_y), \end{aligned} \tag{22}$$

$$\begin{aligned} u^i_{y,0} - u^r_{y,0} &= \frac{\alpha A}{k_{\mathrm{T}}C^0_{66}}(1 + e^{-2i\alpha d})(C_{16}P_x + C_{66}P_y) \\ &\quad + \frac{\beta C}{k_{\mathrm{T}}C^0_{66}}(1 + e^{-2i\beta d})(C_{16}Q_x + C_{66}Q_y). \end{aligned} \tag{23}$$

Subsequently, Eqs. (20) and (21) can be rewritten as

$$\begin{bmatrix} u^i_{x,0} \\ u^i_{y,0} \end{bmatrix} + \begin{bmatrix} u^r_{x,0} \\ u^r_{y,0} \end{bmatrix} = \mathbf{M} \begin{bmatrix} A \\ C \end{bmatrix}, \tag{24}$$

where **M** is defined as

$$\mathbf{M} = \begin{bmatrix} P_x(1-e^{-2i\alpha d}) & Q_x(1-e^{-2i\beta d}) \\ P_y(1-e^{-2i\alpha d}) & Q_y(1-e^{-2i\beta d}) \end{bmatrix}. \tag{25}$$

Similarly, Eqs. (22) and (23) give

$$\begin{bmatrix} u^i_{x,0} \\ u^i_{y,0} \end{bmatrix} - \begin{bmatrix} u^r_{x,0} \\ u^r_{y,0} \end{bmatrix} = \mathbf{N} \begin{bmatrix} A \\ C \end{bmatrix}, \tag{26}$$

where **N** is defined as

$$\mathbf{N} = \begin{bmatrix} \frac{\alpha}{k_L C^0_{11}}(1+e^{-2i\alpha d})(C_{11}P_x + C_{16}P_y) & \frac{\beta}{k_L C^0_{11}}(1+e^{-2i\beta d})(C_{11}Q_x + C_{16}Q_y) \\ \frac{\alpha}{k_T C^0_{66}}(1+e^{-2i\alpha d})(C_{16}P_x + C_{66}P_y) & \frac{\beta}{k_T C^0_{66}}(1+e^{-2i\beta d})(C_{16}Q_x + C_{66}Q_y) \end{bmatrix}. \tag{27}$$

By combining Eqs. (24) and (26), we obtain

$$\begin{bmatrix} u^r_{x,0} \\ u^r_{y,0} \end{bmatrix} = \mathbf{S} \begin{bmatrix} u^i_{x,0} \\ u^i_{y,0} \end{bmatrix}, \tag{28}$$

where the scattering matrix **S** for the reflective wave is expressed by

$$\mathbf{S} = \begin{bmatrix} S_{LL} & S_{TL} \\ S_{LT} & S_{TT} \end{bmatrix}, \tag{29}$$

where S_{LL} (S_{LT}) indicates the amplitude of the reflected longitudinal (transverse) wave when the incident wave is longitudinal [Fig. 1(b)]; and S_{TT} (S_{TL}) denotes the amplitude of the reflected transverse (longitudinal) wave when the incident wave is transverse. Straightforward algebraic manipulations of Eqs. (24), (26), (28), and (29) allow us to express **S** as

$$\begin{bmatrix} S_{LL} & S_{TL} \\ S_{LT} & S_{TT} \end{bmatrix} = \mathbf{M}\left(\frac{\mathbf{M}+\mathbf{N}}{2}\right)^{-1} - \mathbf{I}, \tag{30}$$

where **I** is a second-order unit matrix.

According to derivations in Appendix A, the amplitude of S_{LT} in Eq. (30) can be simplified as

$$|S_{LT}| = C^0_{11}k_L\sqrt{\frac{X_1}{(X_2+X_3)}}, \tag{31}$$

where X_1, X_2, and X_3 are defined as

$$\begin{aligned} X_1 = [&P_y(C_{16}Q_x + C_{66}Q_y)\beta\sin(\alpha d)\cos(\beta d) \\ &- Q_y(C_{16}P_x + C_{66}P_y)\alpha\cos(\alpha d)\sin(\beta d)]^2, \end{aligned} \tag{32}$$

$$\begin{aligned} X_2 = [&(C^0_{66}k_T P_y(C_{11}Q_x + C_{16}Q_y) \\ &- C^0_{11}k_L P_x(C_{16}Q_x + C_{66}Q_y))\beta\sin(\alpha d)\cos(\beta d) \\ &+ (C^0_{11}k_L(C_{16}P_x + C_{66}P_y)Q_x \\ &- C^0_{66}k_T(C_{11}P_x + C_{16}P_y)Q_y)\alpha\cos(\alpha d)\sin(\beta d)]^2, \end{aligned} \tag{33}$$

$$\begin{aligned} X_3 = (P_yQ_x - P_xQ_y)^2[&(C^2_{16} - C_{11}C_{66})\alpha\beta\cos(\alpha d)\cos(\beta d) \\ &+ C^0_{11}C^0_{66}k_Lk_T\sin(\alpha d)\sin(\beta d)]^2. \end{aligned} \tag{34}$$

In particular, when the conditions of $\sin(\alpha d) = \pm 1$ and $\cos(\beta d) = \pm 1$ are satisfied, the value of $|S_{LT}|$ can be maximal. In this case, the expressions for αd and βd can be written as

$$\alpha d = \frac{\pi}{2}, \frac{3\pi}{2}, \frac{5\pi}{2}, \ldots, \frac{(2n+1)\pi}{2} \ (n = 0,\ 1,\ 2, \ldots), \tag{35}$$

$$\beta d = 0, \pi, 2\pi, 3\pi, \ldots, n\pi \ (n = 0,\ 1,\ 2, \ldots). \tag{36}$$

Therefore, for given parameters, the condition of the maximal $|S_{LT}|$ can be defined by

$$(\beta - \alpha)d = \left(n + \frac{1}{2}\right)\pi \quad (n = 0, 1,\ 2, \ldots). \tag{37}$$

Similarly, the amplitude of S_{LL} can be simplified as

$$|S_{LL}| = \sqrt{\frac{Y_1 + Y_2}{(X_2+X_3)}}. \tag{38}$$

where Y_1 and Y_2 are defined as

$$\begin{aligned} Y_1 = [&(-C_{66}^0 k_T P_y (C_{11} Q_x + C_{16} Q_y) - C_{11}^0 k_L P_x (C_{16} Q_x \\ &+ C_{66} Q_y)) \beta \sin(\alpha d) \cos(\beta d) \\ &+ (C_{11}^0 k_L (C_{16} P_x + C_{66} P_y) Q_x + C_{66}^0 k_T (C_{11} P_x \\ &+ C_{16} P_y) Q_y) \alpha \cos(\alpha d) \sin(\beta d)]^2, \end{aligned} \tag{39}$$

and

$$\begin{aligned} Y_2 = [&(C_{11} C_{66} - C_{16}^2)(P_y Q_x - P_x Q_y) \alpha \beta \cos(\alpha d) \cos(\beta d) \\ &+ C_{11}^0 C_{66}^0 k_L k_T (P_y Q_x - P_x Q_y) \sin(\alpha d) \sin(\beta d)]. \end{aligned} \tag{40}$$

Accordingly, for given parameters, the condition of the maximal $|S_{LL}|$ from Eqs. (38) and (39) can be defined by

$$(\beta - \alpha) d = n\pi \ (n = 0,\ 1,\ 2, \ldots). \tag{41}$$

Under L wave incidence, the normalized L-to-L wave reflection is defined as

$$R_{LL} = |S_{LL}|^2. \tag{42}$$

Likewise, under L wave incidence, the normalized L-to-T wave reflection, which is also called the reflective L-to-T mode conversion ratio, can be defined as

$$R_{LT} = \sqrt{\frac{C_{66}^0}{C_{11}^0}} |S_{LT}|^2. \tag{43}$$

Similarly, under T wave incidence, the normalized T-to-T mode reflection is defined as

$$R_{TT} = |S_{TT}|^2, \tag{44}$$

while the normalized T-to-L mode reflection is defined as

$$R_{TL} = \sqrt{\frac{C_{11}^0}{C_{66}^0}} |S_{TL}|^2. \tag{45}$$

For the scattering parameters S_{LL} and S_{LT}, their phase angles θ_{LL} and θ_{LT} can be calculated by

$$\begin{aligned} \theta_{LL} &= 2 \tan^{-1} \left[\frac{\mathrm{Im}(S_{LL})}{\mathrm{Re}(S_{LL}) + \sqrt{[\mathrm{Re}(S_{LL})]^2 + [\mathrm{Im}(S_{LL})]^2}} \right], \\ \theta_{LT} &= 2 \tan^{-1} \left[\frac{\mathrm{Im}(S_{LT})}{\mathrm{Re}(S_{LT}) + \sqrt{[\mathrm{Re}(S_{LT})]^2 + [\mathrm{Im}(S_{LT})]^2}} \right], \end{aligned} \tag{46}$$

where Re and Im represent the real and imaginary parts, respectively.

In theory, R_{LT} should be equal to R_{TL}, and R_{LL} equal to R_{TT}. From the energy conservation perspective, the sum of R_{LL} and R_{LT} should be 1 for L wave incidence. Similarly, the sum of R_{TT} and R_{TL} should also be 1 for T wave incidence.

B. Effective parameters and their effects on the reflection of longitudinal and transverse waves

Using the previously described scattering model, this subsection logically analyzes the effects of the effective parameters on the reflective L and T waves to qualitatively understand the wave reflection and quantitatively characterize the scattering properties. Note that all of the following results are based on the apparent condition of $C_{16}^2 < C_{11} C_{66}$ as illustrated in Eq. (8).

In view of the interface between the two different solid media, it is necessary to respectively set C_{11} and ρ_M of the metamaterial as C_{11}^0 and ρ_0 to ensure that the incident longitudinal wave can completely transmit into the metamaterial. For the solid-solid model in Fig. 1(b), the case of $(C_{11},\ C_{66},\ C_{16}) = (C_{11}^0,\ 0.5C_{11}^0,\ 0.5C_{11}^0)$ is selected as the strong-coupling representative to investigate the scattering parameters S_{LL}, S_{LT}, S_{TT}, and S_{TL}, as shown in Figs. 2(a) and 2(b). An incident longitudinal wave would simultaneously generate reflected longitudinal and transverse waves. The amplitude of the reflected longitudinal wave has an oscillatory variation as a function of the frequency, while the reflected transverse wave exhibits an amplitude larger than 1. This indicates the occurrence of the transverse resonance in the system. Similarly, the longitudinal wave is also excited by an incoming transverse wave incidence. When both C_{66} and C_{16} are fixed to $0.5C_{11}^0$ and C_{11} varies within $[0.75C_{11}^0,\ 2C_{11}^0]$, significant L-to-T conversion takes place near 10 kHz as shown in Figs. 2(c) and 2(d).

Comparing the results illustrated in Figs. 2(c)–2(f), it is observed that the appearance of the phase aberration corresponds exactly to the frequency where R_{LT} and R_{LL} take the maximum and minimum values, respectively. It is well known that phase aberration is a typical feature of resonance. Therefore, the above coincidence implies that it is the resonance that triggers the conversion between the L- and T-mode waves. From the qualitative perspective, the wave motion should be a reflective FP resonance, where the constructive interference of multiply reflected waves occurs in two different solid media.

To further analyze the effect of C_{66}, Figs. 3(a) and 3(b) present the scattering parameters in the case of $C_{66} = C_{11}$. Obviously, the number of the reflection peaks is less than that in Figs. 2(a) and 2(b). This illustrates that a larger C_{66} will result in a higher L-to-T conversion efficiency at higher frequencies provided C_{11} and C_{16} remain unchanged. As shown in Figs. 2(c) and 2(d), below 30 kHz, there is a continuous region, as well as some other scattered regions, where the L-to-T conversion reaches 1.0. Above 30 kHz, only the combinations discretely distributed in the region with $C_{66} < C_{11}$ can produce relatively high L-to-T conversion efficiency. Again, Figs. 3(c)–3(f) show that the maximal R_{LT} and the minimal R_{LL} appear in the case of

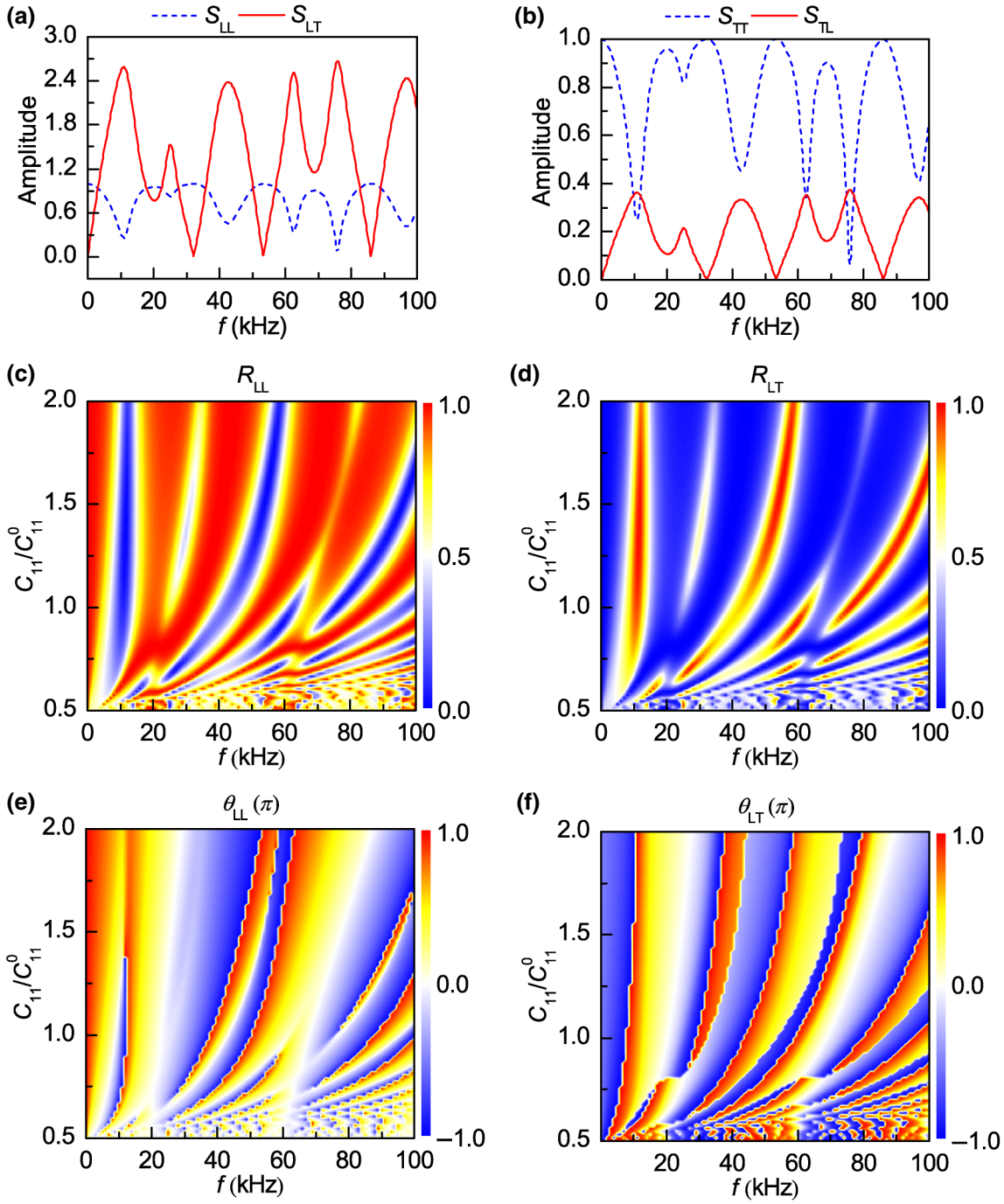

FIG. 2. Characterizations of the scattering matrix and normalized wave reflection with varying C_{11} and f. (a) and (b) Amplitudes of the scattering parameters S_{LL}, S_{LT}, S_{TT}, and S_{TL} when $(C_{11},\ C_{66},\ C_{16}) = (C_{11}^0,\ 0.5C_{11}^0,\ 0.5C_{11}^0)$. (c)–(f) Normalized wave reflection R_{LL} and R_{LT}, (c) and (d), phase angle θ_{LL} and θ_{LT}, (e) and (f), of the scattering parameters S_{LL} and S_{LT} with the variation of C_{11}/C_{11}^0 from 0.501 to 2.0, and f from 10 Hz to 100 kHz for $(C_{66},\ C_{16}) = (0.5C_{11}^0,\ 0.5C_{11}^0)$. Unless otherwise stated, the effective mass density of the metasurface is $\rho_M = \rho_0 = 950$ kg/m^3 and its thickness is set as $d = 2$ cm throughout the paper.

phase aberration, further confirming that the FP resonance indeed causes the reflective L-to-T wave conversion.

To show the role of C_{16}, Figs. 4(a) and 4(b) display the scattering parameters for the representative extreme combination of $(C_{11},\ C_{66},\ C_{16}) = (C_{11}^0,\ C_{11}^0,\ 0.98C_{11}^0)$. Clearly, compared with the previous case, more reflection peaks can be observed no matter whether the incident wave is longitudinal or transverse. This suggests that $C_{11} = C_{66} = C_{16}$ can easily generate more FP resonances within the same frequency range. Moreover, this

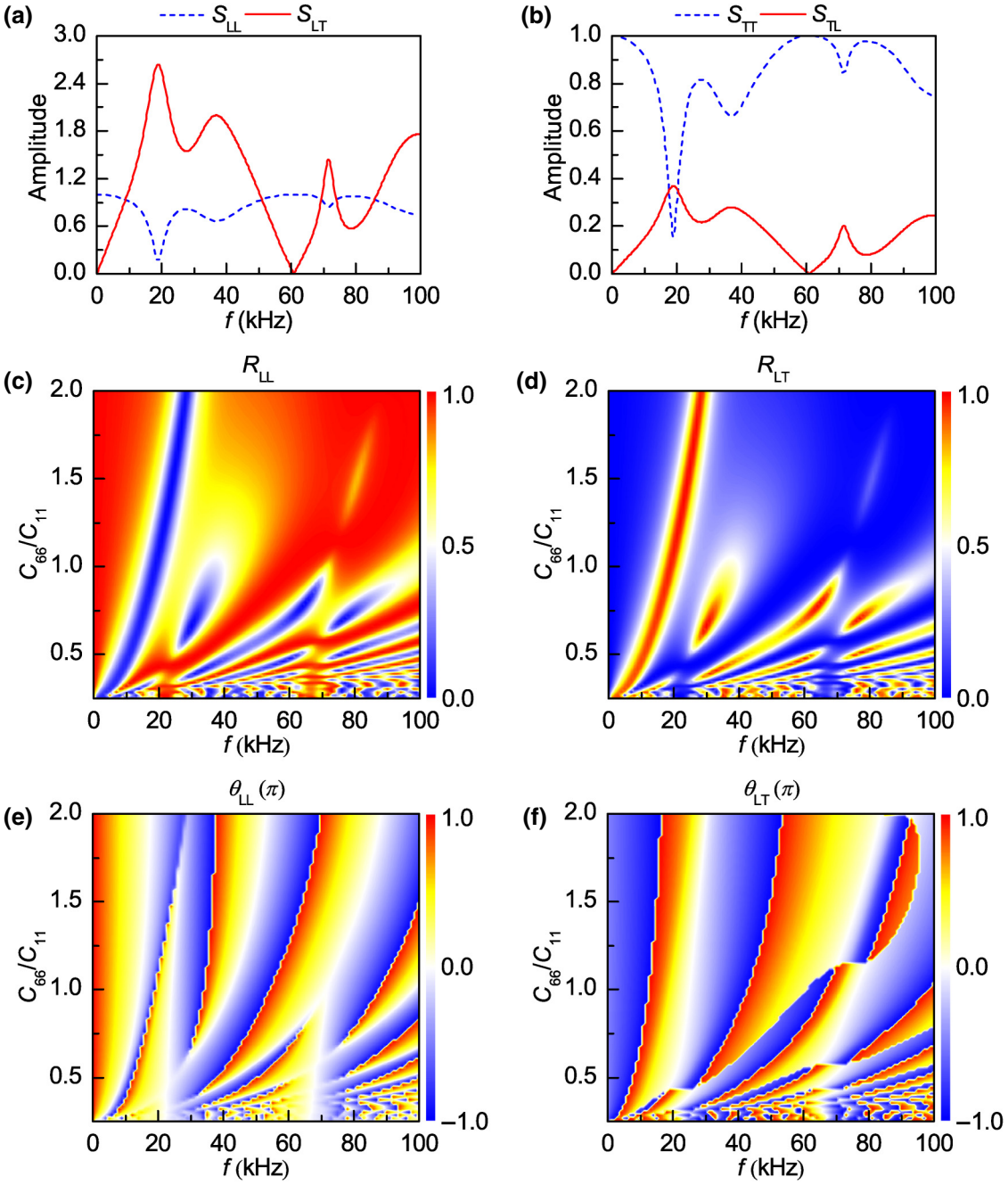

FIG. 3. Dependence of the wave reflection on C_{66} and f under incident L waves. (a) and (b) Amplitudes of the scattering parameters S_{LL}, S_{LT}, S_{TT}, and S_{TL} for $(C_{11},\ C_{66},\ C_{16}) = (C_{11}^0,\ C_{11}^0,\ 0.5C_{11}^0)$. (c)–(f) Normalized wave reflection R_{LL} and R_{LT}, (c) and (d), phase angle θ_{LL} and θ_{LT}, (e) and (f), of scattering parameters S_{LL} and S_{LT} with the variation of C_{66}/C_{11} from 0.251 to 2.0, and f from 10 Hz to 100 kHz for $(C_{11},\ C_{16}) = (C_{11}^0,\ 0.5C_{11}^0)$.

case is more suitable for realizing the low-frequency large reflective L-to-T wave conversion. However, as shown in Figs. 4(c) and 4(d), the maximum R_{LT} occurs in fewer regions. This implies that this extreme parameter combination is harder to realize for maximum wave conversion. As displayed in Figs. 4(e) and 4(f), the phase aberration occurs only in the very low-frequency region when C_{16} approaches C_{11}. Therefore, the presented extreme case in Fig. 4 is a good choice for low-frequency wave conversion.

To show the effect of the effective parameters on the eigenstates, Figs. 5(a) and 5(b) display the polarization angles of the QL and QT modes, respectively. With the increase of C_{66} and C_{16}, θ_{QL} gradually varies from 0° to 45°, while θ_{QT} changes from −90° to −45°. For both θ_{QL} and θ_{QT}, a larger C_{66} will lead to a larger angle if C_{16}

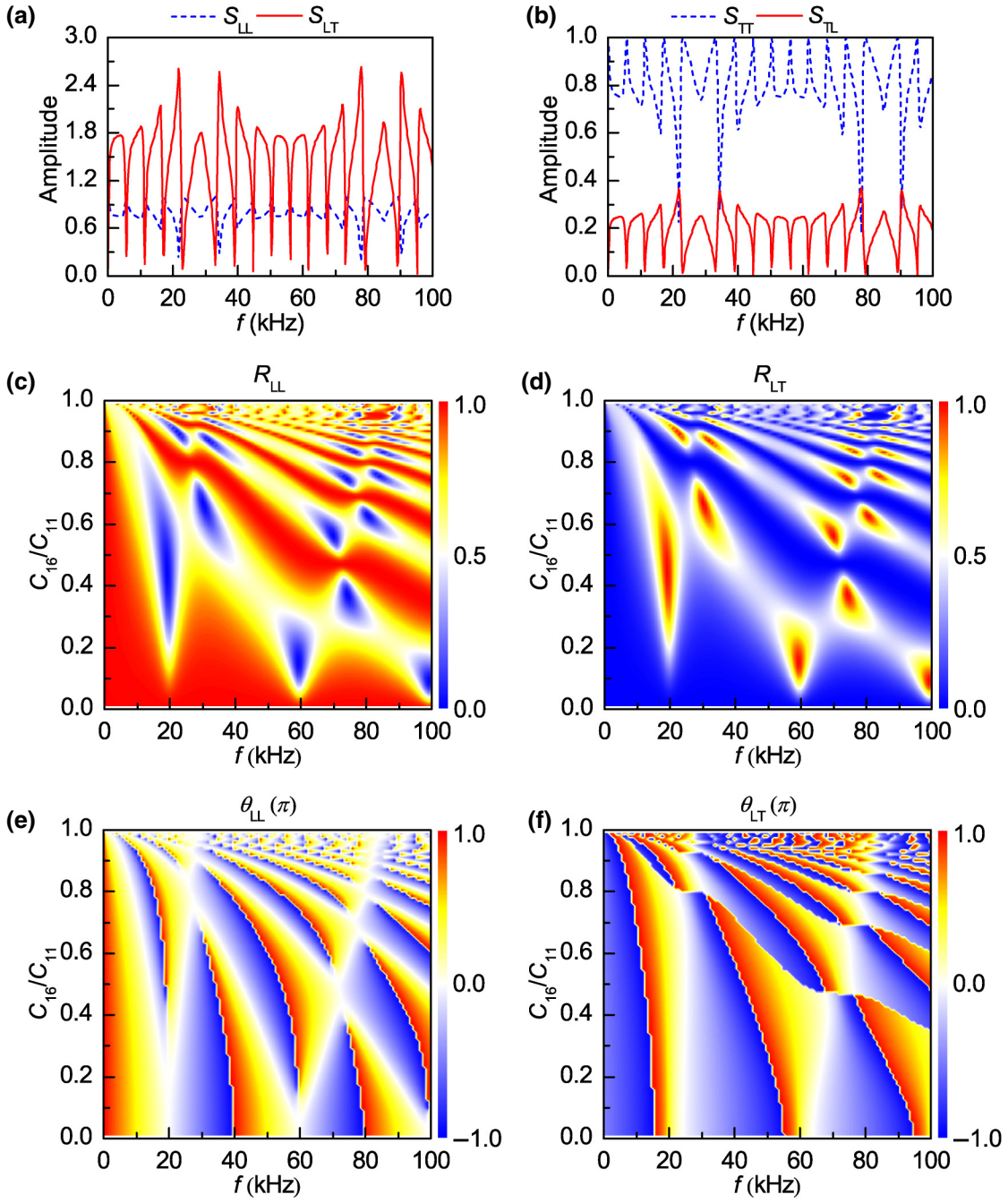

FIG. 4. Dependence of the wave reflections on C_{16} and f under incident L waves. (a) and (b) Amplitudes of the scattering parameters S_{LL}, S_{LT}, S_{TT}, and S_{TL} for $(C_{11},\ C_{66},\ C_{16}) = (C_{11}^0,\ C_{11}^0,\ 0.98C_{11}^0)$. (c)–(f) Normalized reflection power R_{LL} and R_{LT}, (c) and (d), phase angle θ_{LL} and θ_{LT}, (e) and (f), of the scattering parameters S_{LL} and S_{LT} with the variation of C_{16}/C_{11} from 0.01 to 0.99, and f from 10 Hz to 100 kHz for $(C_{11},\ C_{66}) = (C_{11}^0,\ C_{11}^0)$.

remains the same. Similarly, a larger C_{16} can result in a larger angle if C_{66} remains unchanged. Regardless of the way C_{16} is combined with C_{66}, the difference between the two eigenstates should invariably remain at 90°. This coincides exactly with the fundamental orthogonality between two zeroth-order modes. In the case of $(C_{11},\ C_{66},\ C_{16}) = (C_{11}^0,\ C_{11}^0,\ C_{11}^0)$, the polarization angles of the two modes are 45° and −45°. This suggests that the diagonally polarized modes are expected to yield significant L-to-T mode conversion.

C. Reflective longitudinal-to-transverse mode conversion

Based on the above analyses, this subsection aims to explore the mechanism underpinning the reflective L-to-T wave conversion process. The condition for the maximum

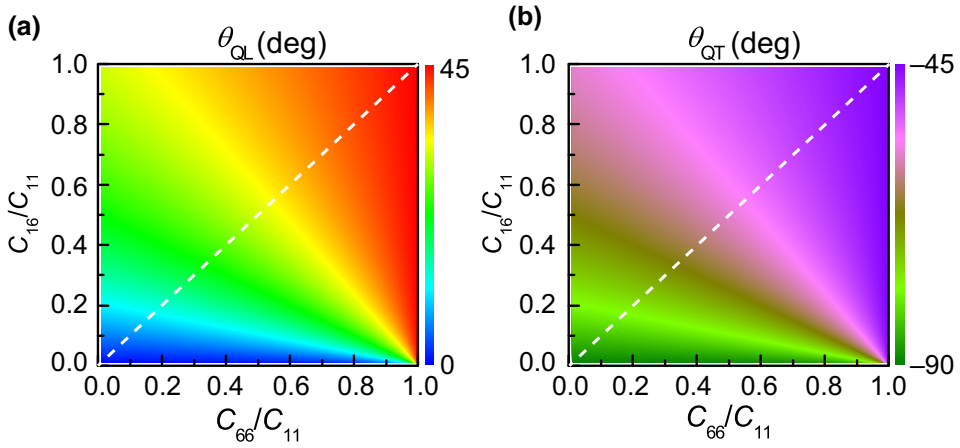

FIG. 5. Characterizations of the polarization angles of the QL and QT modes. (a) θ_{QL} for the combination of (C_{66}/C_{11}, C_{16}/C_{11}) when C_{11} equals C_{11}^0. (b) θ_{QT} for the combination of (C_{66}/C_{11}, C_{16}/C_{11}) when C_{11} equals C_{11}^0. The region below or above the dashed line represents the case of $C_{11}C_{66} > C_{16}^2$ or $C_{11}C_{66} < C_{16}^2$, which means propagating or evanescent waves, respectively.

reflective L-to-T wave conversion is revealed through theoretical analyses and numerical simulations. On this basis, the theory can predict the reflective FP resonance frequency for arbitrary parameter combinations.

1. Condition for the maximum mode conversion

Considering the coexistence of longitudinal and transverse waves, their phase difference may affect the scattering features of the metamaterial. To explore this relationship, Fig. 6(a) shows the effect of the phase difference $\Delta\phi$ on R_{LL} and R_{LT} when $(C_{11}, C_{66}, C_{16}) = (C_{11}^0, 0.5C_{11}^0, 0.5C_{11}^0)$. Both the R_{LL} and R_{LT} curves exhibit multiple peaks. For particular phase differences of 0.5π, 1.5π, 2.5π, 3.5π, 5.5π, 7.5π, and 9.5π, R_{LT} becomes nearly 100%. However, R_{LL} can be close to 100% for 0, π, 2π, 3π, 4π, 5π, 6π, 7π, 8π, 9π, and 10π. As shown in Figs. 6(b) and 6(c), both R_{LL} and R_{LT} reach their extreme values intermittently. Figure 6(d) shows that the maximal R_{LT} only occurs at 2.5π for $C_{11} < C_{66}$. However, the case of the extreme combination in Fig. 6(g) produces two peaks at 3.5π and 5.5π. The similar interval maximal values are observed in Figs. 6(e), 6(f), 6(h), and 6(i).

Obviously, these extreme peaks are produced by the reflective FP resonances and thus induce the maximal L-to-T wave conversion. Combining this phenomenon with Eq. (8), the condition that ensures reflective FP resonance for generating the maximal reflective L-to-T conversion can be established as

$$\Delta\phi = (\beta - \alpha)d = \left(m + \frac{1}{2}\right)\pi, \quad (m = 0,1,2,\ldots). \tag{47}$$

However, if the condition of $\Delta\phi = m\pi$ $(m = 0,\ 1,\ 2,\ldots)$ is satisfied, the unimodal FP resonance will generate the 100% reflection of longitudinal waves. Interestingly, these two conditions perfectly match with Eqs. (37) and (41).

2. Reflective mode-conversion Fabry-Perot resonance frequency

According to Eqs. (8) and (36), the reflective mode-conversion FP resonance frequency is defined as

$$f_{LT} = \frac{[m + (1/2)]}{2d\left\{\sqrt{\frac{\rho_M\left[C_{11} + C_{66} + \sqrt{(C_{11}-C_{66})^2+4C_{16}^2}\right]}{2(C_{11}C_{66}-C_{16}^2)}} - \sqrt{\frac{\rho_M\left[C_{11} + C_{66} - \sqrt{(C_{11}-C_{66})^2+4C_{16}^2}\right]}{2(C_{11}C_{66}-C_{16}^2)}}\right\}} \quad (m = 0,1,2,\ldots). \tag{48}$$

Figure 7 displays the effect of the three effective parameters on the first-order f_{LT}. Assuming $C_{11} = C_{11}^0$ or $C_{66} = C_{11}^0$, the lowest f_{LT} is generated when C_{16} equals to C_{11} and C_{66}. Similarly, f_{LT} decreases when C_{16} is close to C_{11} and C_{66}. When C_{16}, C_{66}, and C_{11} all become small simultaneously, f_{LT} significantly increases from hundreds of hertz to dozens of kilohertz. In short, under the premise of $C_{11}C_{66} > C_{16}C_{16}$, the first-order f_{LT} is very small and close

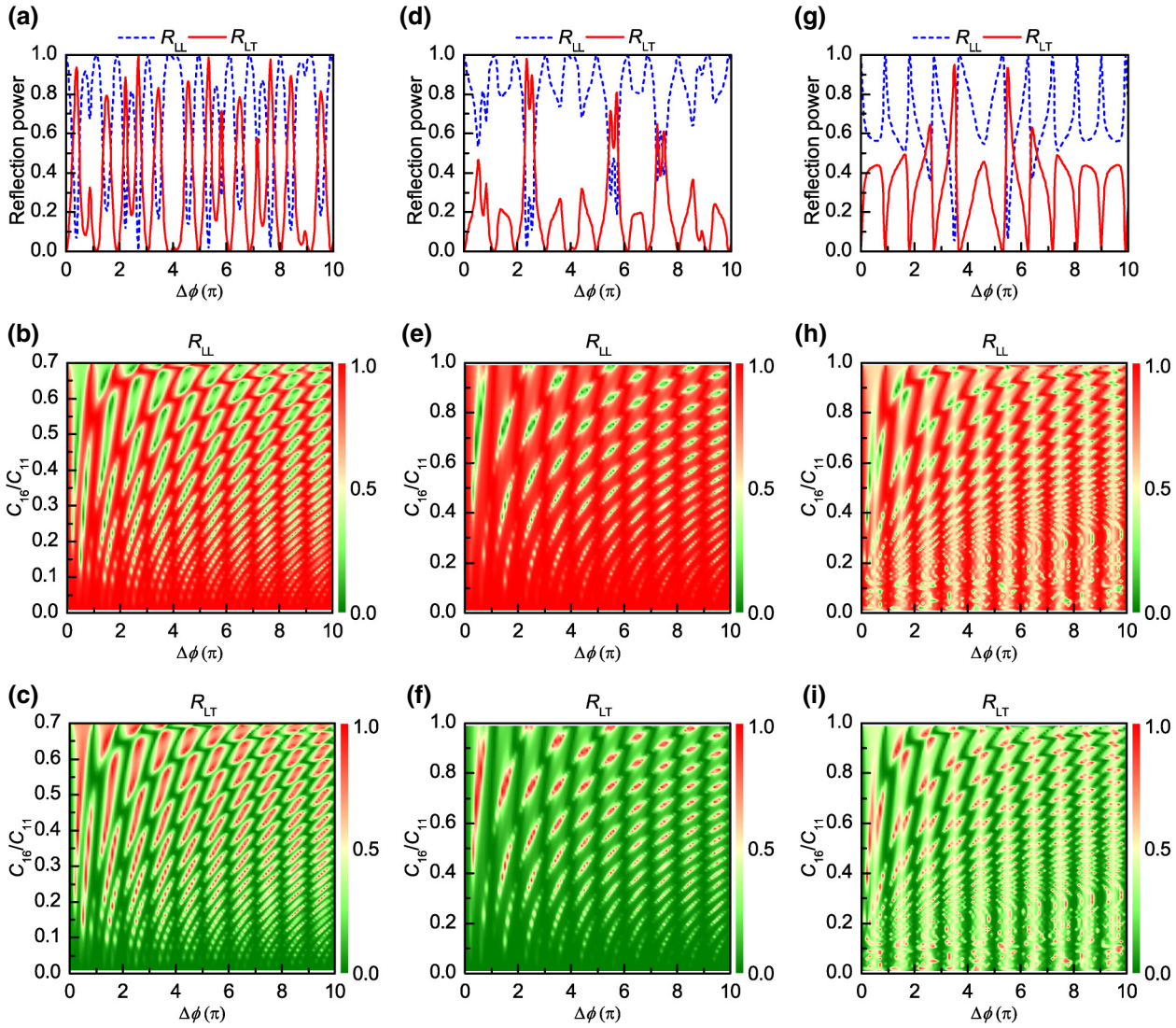

FIG. 6. Effects of the phase difference and effective parameters on the L-to-T wave conversion. (a) Normalized wave reflection R_{LL} (R_{LT}) of the scattering parameter S_{LL} (S_{LT}) as a function of the phase difference $\Delta\phi$ between the QT (β) and QL (α) modes for the effective parameter combination of $(C_{11},\ C_{66},\ C_{16}) = (C_{11}^0,\ 0.5C_{11}^0,\ 0.5C_{11}^0)$. (b) and (c) Contours of R_{LL} and R_{LT} with varying C_{16}/C_{11} for $(C_{11},\ C_{66}) = (C_{11}^0,\ 0.5C_{11}^0)$. (d) Normalized wave reflection R_{LL} and R_{LT} for $(C_{11},\ C_{66},\ C_{16}) = (0.5C_{11}^0,\ C_{11}^0,\ 0.5C_{11}^0)$. (e) and (f) Contours of R_{LL} and R_{LT} for $(C_{11},\ C_{66}) = (0.5C_{11}^0,\ C_{11}^0)$. (g) Normalized wave reflection R_{LL} and R_{LT} for $(C_{11},\ C_{66},\ C_{16}) = (C_{11}^0,\ C_{11}^0,\ 0.98C_{11}^0)$. (h) and (i) Contours of R_{LL} and R_{LT} for $(C_{11},\ C_{66}) = (C_{11}^0,\ C_{11}^0)$.

to 0 when $C_{16}C_{16}$ approaches $C_{11}C_{66}$. The resonance frequency is highly sensitive to the combination of effective parameters.

To sum up, a scattering model based on anisotropic elastic metamaterials is established in this section to investigate the effects of the constitutive parameters on the L-to-T wave conversion. Abundant numerical results show that the maximal reflective L-to-T conversion can be generated through the mechanism of FP resonance. When C_{11} equals C_{66} and C_{16} infinitely approaches C_{11}, the metamaterial can induce ultralow-frequency and high-efficiency L-to-T conversion provided C_{11} is the same as the longitudinal modulus of the background solid.

III. INVERSE DESIGN OF ULTRATHIN ANISOTROPIC REFLECTIVE METASURFACE

Since the design of the metasurface involves controlling multiple parameters, which is difficult to realize using existing metamaterial architectures, here we deploy an inverse-design strategy that offers much greater design freedom and flexibility. Based on scattering theory and the model established in Sec. II on anisotropic metasurfaces, we apply topology optimization [8,9,24,25] to achieve the inverse design of the elastic metamaterials. As shown in Fig. 8(a), with the same objective of transforming the incident longitudinal wave into a reflected transverse wave

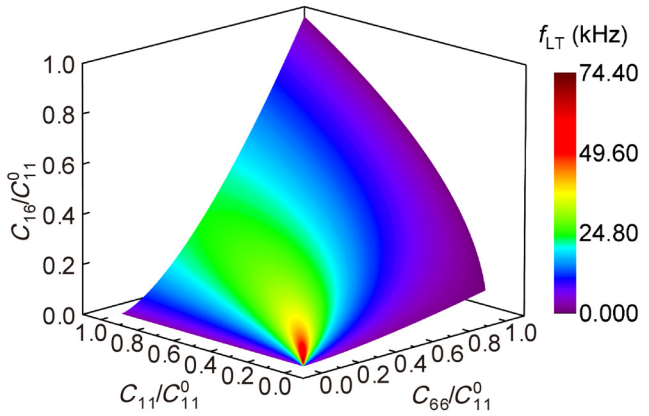

FIG. 7. Prediction of the first-order reflective FP resonance frequency. The first-order f_{LT} changes with the combination of C_{11}, C_{66}, and C_{16}.

for underwater applications, we investigate a metasurface composed of periodic asymmetric microstructures illustrated in Fig. 8(b). Using the dynamic effective medium theory, the microstructure with an arbitrary topology can be equivalent to an anisotropic solid with specific effective constitutive parameters (Appendix B), see Fig. 8(c). Note that the solid areas with a certain thickness in the left and right edges have to be fixed in the optimization to solve the following two issues. Firstly, the thin boundaries result in apparent local vibrations, thereby making it difficult to calculate the effective parameters using the present linear dynamic effective medium theory. Secondly, to guarantee that the coating layer can be directly fixed on the surface of the equipment, it is necessary to ensure the architectural boundaries have intact solid areas to be used for the adhesive or screw fixation. In such situations, the metasurface can not only realize the ideal underwater sound absorption, but also satisfy the fabrication and installation requirements imposed by practical applications.

A. Optimization model of reflective metasurfaces with arbitrary effective parameters

To characterize the difference between the actual effective parameters and the targeted material properties, the characteristic physical quantities, C_{11}, C_{66X}, C_{66Y}, C_{16}, ρ_{11}, and ρ_{22} can be described by

$$\eta_{C_{11}} = \max_{\forall i \subset (1,2,\ldots,N_F)} \left\{ 1 - \frac{\min[C_{11}(i),\ C_{11}^*]}{\max[C_{11}(i),\ C_{11}^*]} \right\}, \tag{49}$$

$$\eta_{C_{66X}} = \max_{\forall i \subset (1,2,\ldots,N_F)} \left\{ 1 - \frac{\min[C_{66X}(i),\ C_{66}^*]}{\max[C_{66X}(i),\ C_{66}^*]} \right\}, \tag{50}$$

$$\eta_{C_{66Y}} = \max_{\forall i \subset (1,2,\ldots,N_F)} \left\{ 1 - \frac{\min[C_{66Y}(i),\ C_{66}^*]}{\max[C_{66Y}(i),\ C_{66}^*]} \right\}, \tag{51}$$

$$\eta_{C_{16}} = \max_{\forall i \subset (1,2,\ldots,N_F)} \left\{ 1 - \frac{\min[C_{16}(i),\ C_{16}^*]}{\max[C_{16}(i),\ C_{16}^*]} \right\}, \tag{52}$$

$$\eta_{\rho_{11}} = \max_{\forall i \subset (1,2,\ldots,N_F)} \left\{ 1 - \frac{\min[\rho_{11}(i),\ \rho^*]}{\max[\rho_{11}(i),\ \rho^*]} \right\}, \tag{53}$$

$$\eta_{\rho_{22}} = \max_{\forall i \subset (1,2,\ldots,N_F)} \left\{ 1 - \frac{\min[\rho_{22}(i),\ \rho^*]}{\max[\rho_{22}(i),\ \rho^*]} \right\}, \tag{54}$$

where η is the defined difference between the targeted and actual values for an intrisic parameters; N_F denotes the number of the uniformly distributed discrete sampling frequencies within the frequency range $f_{\min}$–$f_{\max}$; C_{11}^*, C_{66}^*, C_{16}^*, and ρ^* are the prescribed constitutive parameters of the metasurface.

Theoretically, the inverse design of a customized metasurface has to satisfy various demands of physical features simultaneously. In principle, the effective impedance of the metasurface should be matched with the background solid to make the longitudinal wave completely incident onto the metasurface. Additionally, the metasurface should be designed with the customized mode coupling and anisotropy extent through a unitive optimization model. In particular, the anisotropy implies no distinct structural symmetry. To guarantee the visualized wave motion, the equal condition of ρ_{11} and ρ_{22} is forced during optimization. For the retrieval of effective shear modulus, the strong anisotropy usually causes apparent local boundary rotation vibrations, which in principle would require the high-order dynamic effective medium theory. For the sake of simplicity, it is necessary to ensure the same values of C_{66X} and C_{66Y}. Finally, to guarantee manufacturability and strength, the size of the local minimal solid parts in the microstructure should be larger than a feasible geometrical dimension. Therefore, the topology optimization formulation of an anisotropic elastic reflective metasurface is mathematically defined as,

$$\text{for } \Omega_D = [\chi_1,\ \chi_2,\ \chi_3, \ldots, \chi_i], \quad (i = 1,\ 2, \ldots, N \times N) \tag{55}$$

$$\text{minimize } O(\Omega_D) = \max(\eta_{C_{11}},\ \eta_{C_{66X}},\ \eta_{C_{66Y}},\ \eta_{C_{16}},\ \eta_{\rho_{11}},\ \eta_{\rho_{22}}), \tag{56}$$

$$\text{subject to } \chi_i = \{0,\ 1\}, \tag{57}$$

$$\min_{\Omega_D}(w) \geq w_0, \tag{58}$$

where Ω_D is the design domain displayed in Fig. 8(b); χ_i represents the material phase that declares the solid (1) or air (0) attribute of a pixel in the design domain; $N \times N$ is the number of pixels; O is the objective function of the optimization problem; $\boldsymbol{w}$ signifies the geometrical

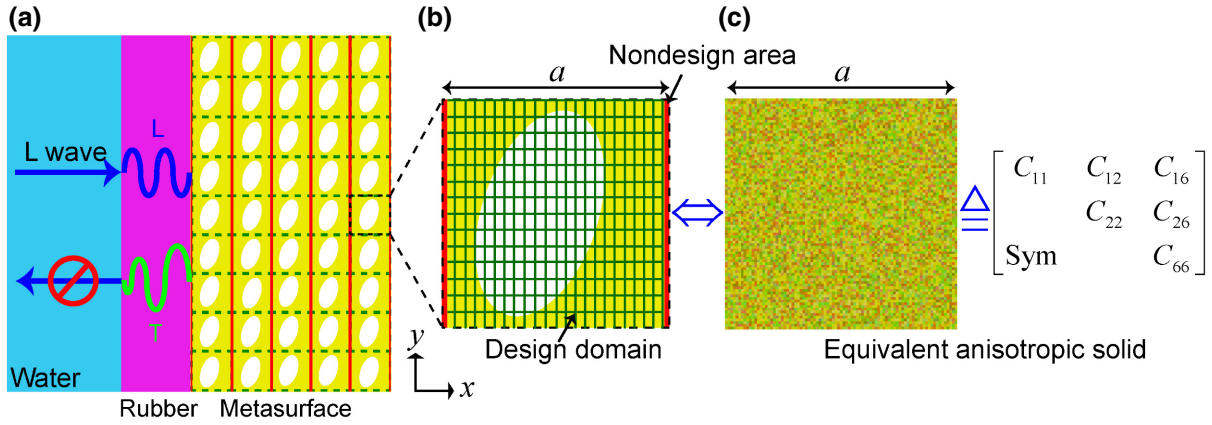

FIG. 8. Schematic of an anisotropic elastic metasurface designed by topology optimization. (a) Model of the incident underwater L wave propagating in a layer of rubber and the anisotropic metasurface. The L-to-T wave conversion within the metasurface generates the reflective T wave excited by the incident L wave. (b) A metasurface microstructure whose left and right boundaries, marked by red regions, are nondesign domains of the homogeneous solid during topology optimization. The design domain of the topology optimization is composed of a certain number of pixels. (c) An equivalent elastic anisotropic solid with the effective elasticity matrix constituting nine nonzero components.

vector consisting of all local solid sizes; and w_0 is a prescribed value suggested by numerical tests. In short, the inverse-designed metasurfaces with customized constitutive parameters can be gradually acquired through the unified optimization theory and model.

B. Optimized reflective metasurfaces with customized mode coupling

In this subsection, nine representative reflective metasurfaces are inversely designed and systematically characterized in terms of their scattering properties. To obtain an arbitrary anisotropy extent, no structural symmetry is considered during optimization. The parameters of the isotropic background solid are chosen as: $\rho_0 = 950$ kg/m^3, $C_{11}^0 = 2.369$ GPa, and the Poisson's ratio $\nu = 0.49$. The metasurface is made of vacuum and aluminum (Al) whose parameters are $\rho_{\mathrm{Al}} = 2700$ kg/m^3, the Young's modulus $E_{\mathrm{Al}} = 0.71$ GPa, and the Poisson's ratio $\nu_{\mathrm{Al}} = 0.33$. The lattice constant of the metasurface is 1 cm. Throughout the paper, the thickness of the metaconverter is selected as 2 cm. The left and right edges of a microstructural domain is made of an $a/40$-thick Al layer, where a is the lattice constant. Here the genetic algorithm [8,9,24,25] is adopted to solve the optimization problem in Eqs. (53)–(56). The prescribed minimal geometrical size w_0 is $a/40$. The microstructural domain is divided into 80×80 pixels. The genetic parameters of optimization are the crossover probability $P_C = 0.9$, the mutation probability $P_M = 0.03$, the population size $N_P = 90$, and the tournament competition group $N_{\mathrm{ts}} = 63$. All inverse-design calculations are executed on a Linux cluster with Intel Xeon Platinum 8168 @ 2.70 GHz via MPI parallel technology. One whole optimization process contains 4000 generations, which takes about 111.3 h. All the retrievals of the effective parameters and calculations of the eigenstates are accomplished by the commercial finite element software ABAQUS 6.14–1. The transient- and steady-state wave propagation simulations are conducted by COMSOL Multiphysics 5.3.

From the optimized topology shown in Fig. 9(a), for the extreme effective parameter combination of $(C_{11}, C_{66}, C_{16}) = (C_{11}^0, C_{11}^0, 0.98C_{11}^0)$, the inverse-designed metasurface contains several asymmetric solid blocks that are mutually connected through relatively thin rods. Figure 9(b) shows that the metasurface can generate the intrinsic QT and QL modes with the polarization angles of $-45°$ and $45°$, respectively. These angles precisely match the predictions of the polarization angles in Fig. 5. On one hand, this coincidence demonstrates the correctness of the scattering theory established in Sec. II. On the other hand, the metasurface is proved to exhibit the correct required C_{11}, C_{66}, and C_{16}. As for the effective parameters, the metasurface $M1$ indeed has identical ρ_{11} and ρ_{22} equal to 950 kg/m^3 as depicted in Fig. 9(c). The effective moduli in Figs. 9(d) and 9(e) demonstrate that the targeted C_{11}, C_{66}, and C_{16} are achieved. However, C_{22} is much larger than C_{11}, meaning that the metasurface exhibits very strong anisotropy. The obvious difference between C_{16} and C_{26} further indicates the anisotropic nature of the metasurface.

To verify the scattering properties of the metasurface $M1$, Figs. 10(a) and 10(b) compare the results from the theoretical scattering theory and the computed scattering features of $M1$, showing an overall consistency between them. However, resonance frequencies differ. Very interestingly, the optimized curves match very well with the theoretical ones when C_{16} is adjusted to $0.977C_{11}$, as shown in Figs. 10(c) and 10(d). The adjustment is

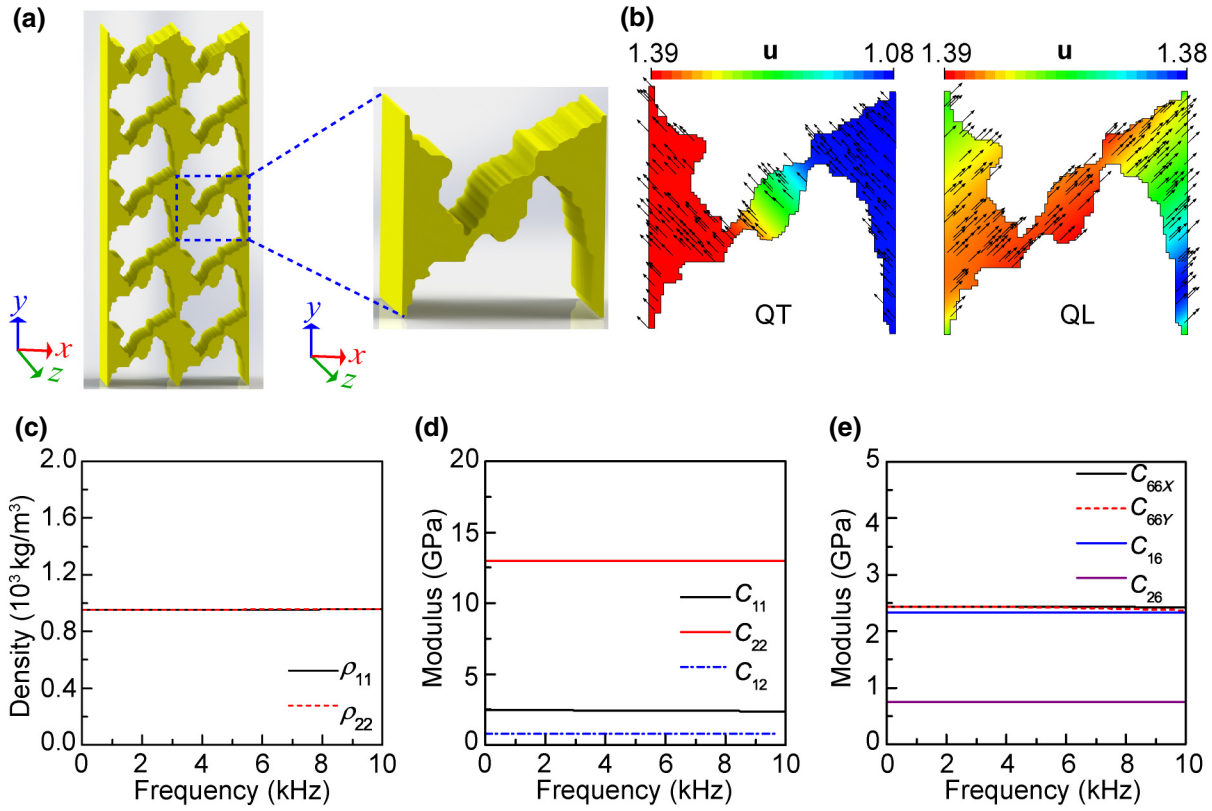

FIG. 9. Characterizations of a representative inverse-designed elastic anisotropic metasurface. (a) An optimized metasurface $M1$ for $(C_{11},\ C_{66},\ C_{16}) = (C_{11}^0,\ C_{11}^0,\ 0.98C_{11}^0)$. (b) Displacement fields $\mathbf{u} = (u_x, u_y)$ of the QT and QL modes. Arrows represent the direction of the polarizations and the particle vibration amplitude. (c) Effective mass densities ρ_{11} and ρ_{22}. (d) Effective elastic moduli C_{11}, C_{22}, and C_{12}. (e) Effective elastic moduli C_{66X}, C_{66Y}, C_{16}, and C_{26}. Without particular indication, the effective mass density of the metasurface throughout the paper is selected as $\rho = 950$ kg/m^3. The metasurface is composed of two layers and its thickness is set as $d = 2$ cm.

consistent with the results obtained from optimization, where there is a small difference compared with the required values. This demonstrates the correctness of the scattering properties of the metasurface $M1$. Figures 10(e) and 10(f) present the displacement fields of the whole solid-solid model at 2700 Hz and 6100 Hz, respectively. When R_{LT} takes a certain value larger than 0.2, the displacement field of the background solid is dominated by the transverse wave modes coupled with longitudinal wave modes to a certain extent. When R_{LT} approaches zero, the reflected wave motion turns into the nearly pure longitudinal wave accompanied by a weak transverse wave. Conversely, for a 2700-Hz transverse wave, the reflected wave field is dominated by the longitudinal wave coupled with a small degree of transverse wave. However, the incident transverse wave mainly causes the reflected transverse wave at 6100 Hz. This also confirms the very small R_{LT} in Fig. 10(d). Regardless of the operating frequency, the metasurface layer vibrates along the oblique direction.

To show the effects of the effective parameters on the topology and the scattering properties, Fig. 11 displays the layouts of some representative optimized metasurfaces. Overall, all metasurfaces have several asymmetric solid blocks and relatively narrow rods. With the change of effective parameters, some voids are generated within the solid block, thus reducing the value of C_{16}. Compared with $M1$ and $M2$, the R_{LT} of $M3$ decreases with increasing frequency. This means that, with fixed C_{11} and C_{66}, reducing C_{16} can directly compromise the L-to-T wave conversion efficiency. Below 4000 Hz, the R_{LT} of $M1$ is larger than that of the other two structures. The conversion property of $M5$ is the same as that of $M3$. However, it is worth noting that the conversion efficiencies of both $M4$ and $M6$ are higher than that of $M1$. In particular, metasurface $M6$ has the salient broadband nature. However, in the low-frequency region below 1000 Hz, $M1$ allows the largest conversion among all considered metasurfaces. Therefore, this indicates that $M1$ could be the best choice for the ideal low-frequency L-to-T wave conversion. However, $M4$ and $M6$ are better to realize the broadband L-to-T wave conversion. The results and discussions of some other inverse-designed metasurfaces are presented in Appendix C.

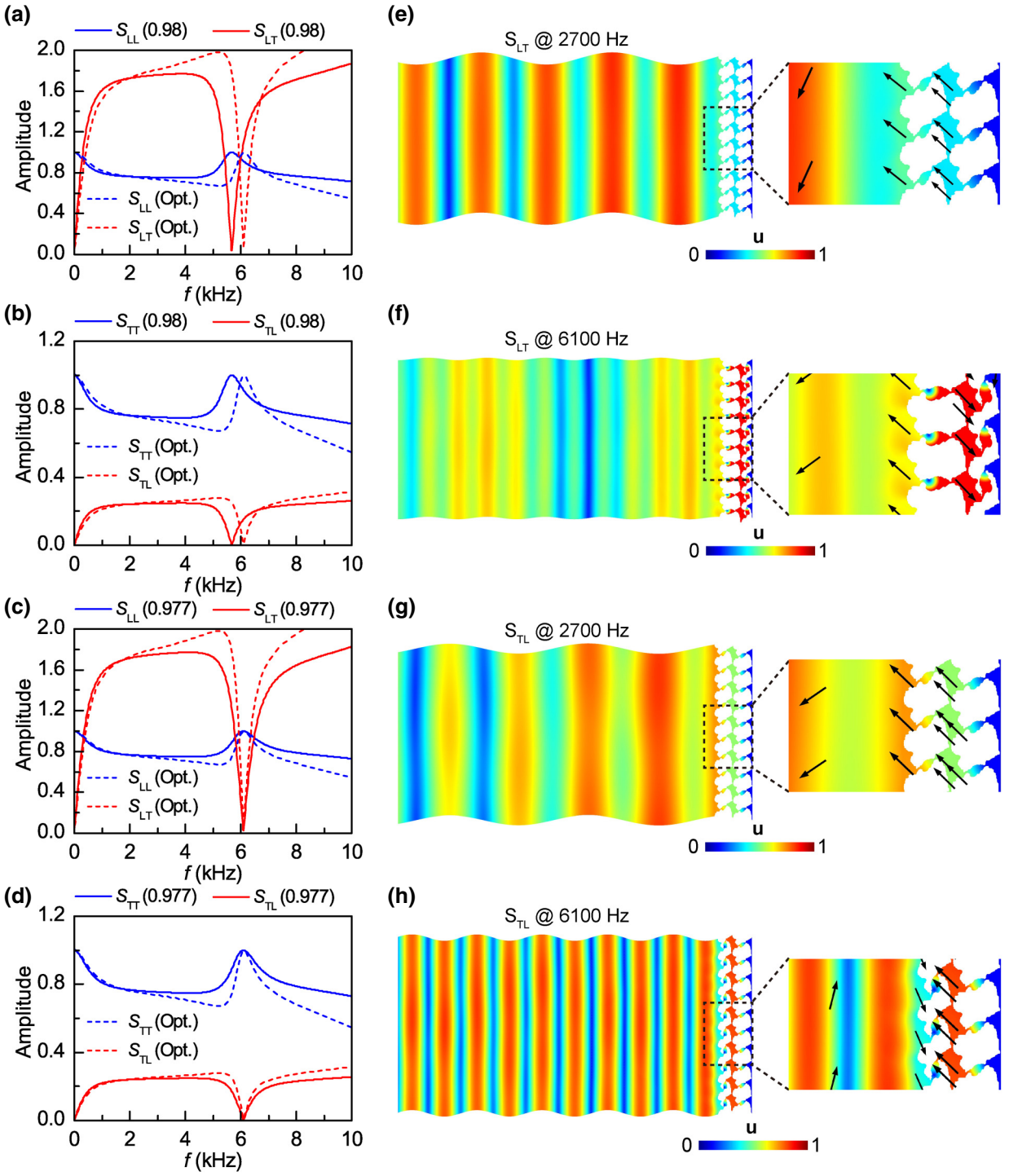

FIG. 10. Scattering properties of the metasurface $M1$ in Fig. 9. (a) and (b) Amplitudes of the scattering parameters S_{LL}, S_{LT}, S_{TT}, and S_{TL} for optimized (Opt.) structure and theoretical combination of $(C_{11},\ C_{66},\ C_{16}) = (C_{11}^0,\ C_{11}^0,\ 0.98C_{11}^0)$. (c) and (d) Scattering parameters for the optimized structure (Opt.) and theoretical model with the combination of $(C_{11},\ C_{66},\ C_{16}) = (C_{11}^0,\ C_{11}^0,\ 0.977C_{11}^0)$. Solid and dashed lines indicate the theoretical and optimized results, respectively. (e) and (f) Displacement fields $\mathbf{u} = (u_x,\ u_y)$ for S_{LT} under the incident longitudinal wave at 2700 Hz (e) and 6100 Hz (f). (g) and (h) Displacement fields for S_{TL} under the incident transverse wave at 2700 Hz (g) and 6100 Hz (h).

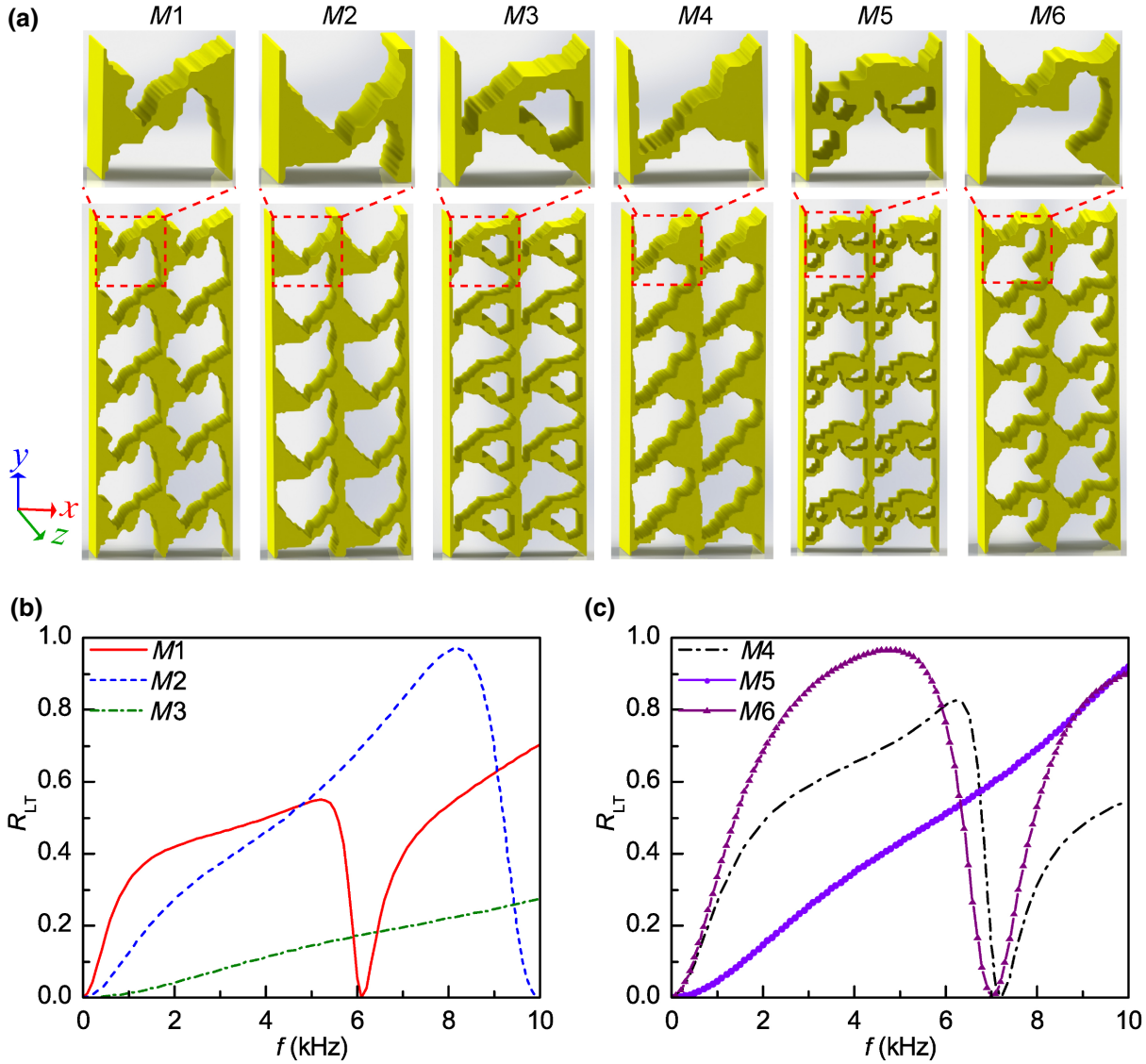

FIG. 11. Comparison of the topologies and normalized reflection energy for the inverse-designed metasurfaces $M1$–$M6$. (a) Topologies for different targeted effective parameter combinations. (b) and (c) Normalized wave reflection R_{LT} with frequency of different metasurfaces. Targeted effective parameters are $M1$, $(C_{11}, C_{66}, C_{16}) = (C_{11}^0, C_{11}^0, 0.98C_{11}^0)$; $M2$, $(C_{11}, C_{66}, C_{16}) = (C_{11}^0, C_{11}^0, 0.7C_{11}^0)$; $M3$, $(C_{11}, C_{66}, C_{16}) = (C_{11}^0, C_{11}^0, 0.5C_{11}^0)$; $M4$, $(C_{11}, C_{66}, C_{16}) = (C_{11}^0, 0.5C_{11}^0, 0.67C_{11}^0)$; $M5$, $(C_{11}, C_{66}, C_{16}) = (C_{11}^0, 0.5C_{11}^0, 0.5C_{11}^0)$; and $M6$, $(C_{11}, C_{66}, C_{16}) = (C_{11}^0, 0.3C_{11}^0, 0.5C_{11}^0)$, respectively.

To clearly show the entire wave propagation process, we conduct numerical simulations in the time domain, and Fig. 12 presents the process, displaying the L-to-T conversion and the reflected longitudinal and transverse waves after the longitudinal wave is incident on the background solid shown in Fig. 12(a). As shown in Fig. 12(b), the incident longitudinal wave causes the resonance of the metasurface and then generates the transverse wave mode. Then the conversion gives rise to the reflected longitudinal and transverse waves simultaneously. From the transient wave fields in Figs. 12(b)–12(d), it is observed that the longitudinal wave is preferentially reflected from the interface between the background solid and the metasurface at a faster speed. Subsequently, the transverse wave is also reflected from the interface. As for the whole transient wave propagation process, please see in the Supplemental Material Videos S1 and S2 in Ref. [26].

To further confirm the maximal L-to-T wave conversion in Fig. 11, Fig. 13 illustrates the corresponding displacement fields at four representative frequencies. Clearly, these steady-state dynamic responses are dominated by the transverse wave modes, while coupled with weak longitudinal wave modes. In all dynamic responses, the metasurface vibrates along a similar oblique direction. The displacement fields show the different levels of coupling wave modes. Compared with the other three metasurfaces,

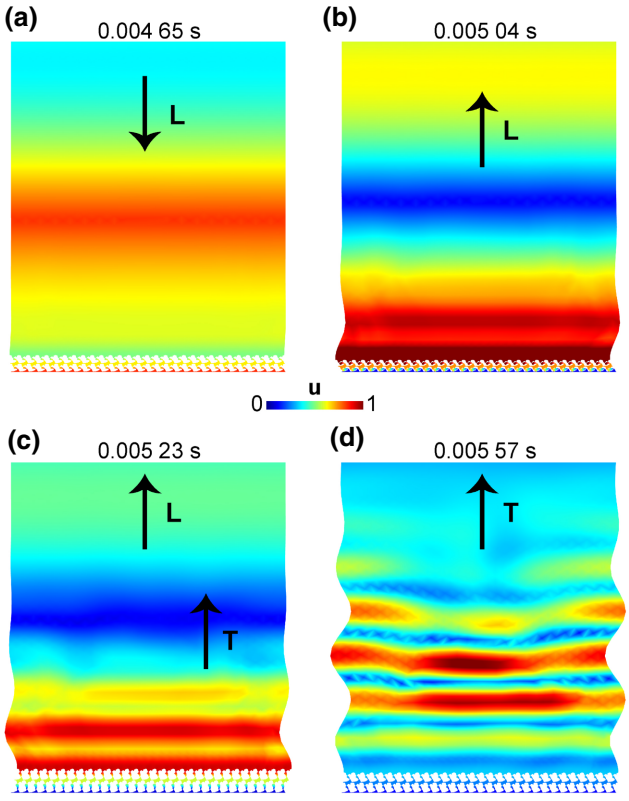

FIG. 12. (a)–(d) Time-domain simulation of wave propagation process based on metasurface $M1$. A longitudinal wave is incident from the background isotropic solid and then causes the mode conversion and reflection. The symbols L and T represent the longitudinal and transverse waves, respectively.

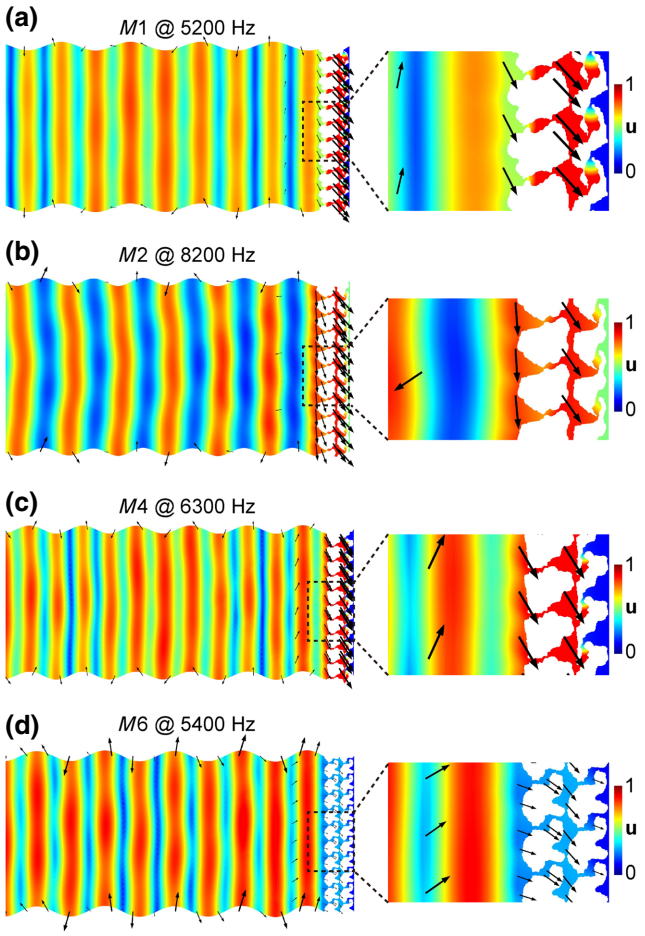

FIG. 13. Displacement fields with the maximal R_{LT} for the four representative metasurfaces. (a)–(d) The maximal R_{LT} values of the metasurfaces $M1$ (a), $M2$ (b), $M4$ (c), and $M6$ (d) are determined within 0.5 Hz–10 kHz. The incident L wave is applied on the left edge of the solid-solid model illustrated in Fig. 1(b).

$M1$ allows for a purer transverse wave mode. This implies that the metasurface $M1$ can generate the wave motion approaching the purest transverse wave mode, even though the R_{LT} at a low frequency is smaller than that at relatively higher frequencies. The higher the resonance frequency means the higher coupling extent of the longitudinal wave.

IV. UNDERWATER SOUND ABSORPTION USING OPTIMIZED REFLECTIVE METASURFACES

We hypothesize that our designed elastic reflective metasurfaces could realize underwater acoustic wave manipulation in different ways, and in particular could achieve effective underwater sound absorption as presented schematically in Fig. 14(a). Practically and qualitatively, the incident wave from water is transmitted to both the viscoelastic layer and the metasurface. The latter reflectively converts the L wave into T waves, which get trapped and dampened in the viscoelastic layer. To demonstrate the absorption mechanism using the bilayer system, Fig. 14(b) presents the underwater absorption by the bilayer system. The acoustic absorption can be quantified from the reflected wave in water by

$$\chi_A = 1 - |R|^2, \tag{59}$$

where R denotes the reflection coefficient.

From the results in Fig. 14(b), the absorption curve of the metasurface $M1$ matches well with that from the theoretical model based on the homogenized effective medium theory with the targeted effective parameters. Although absorption at high frequencies shows a slight difference, the overall features of the absorption curves are very close to each other. In particular, they are almost identical in the low-frequency range below 6 kHz. This evidently demonstrates the efficacy of the optimized design. Compared with the pure rubber layer, the introduction of a metasurface effectively enables 100% absorption at 2700 Hz. It is worth noticing that the absorption ability is closely related to

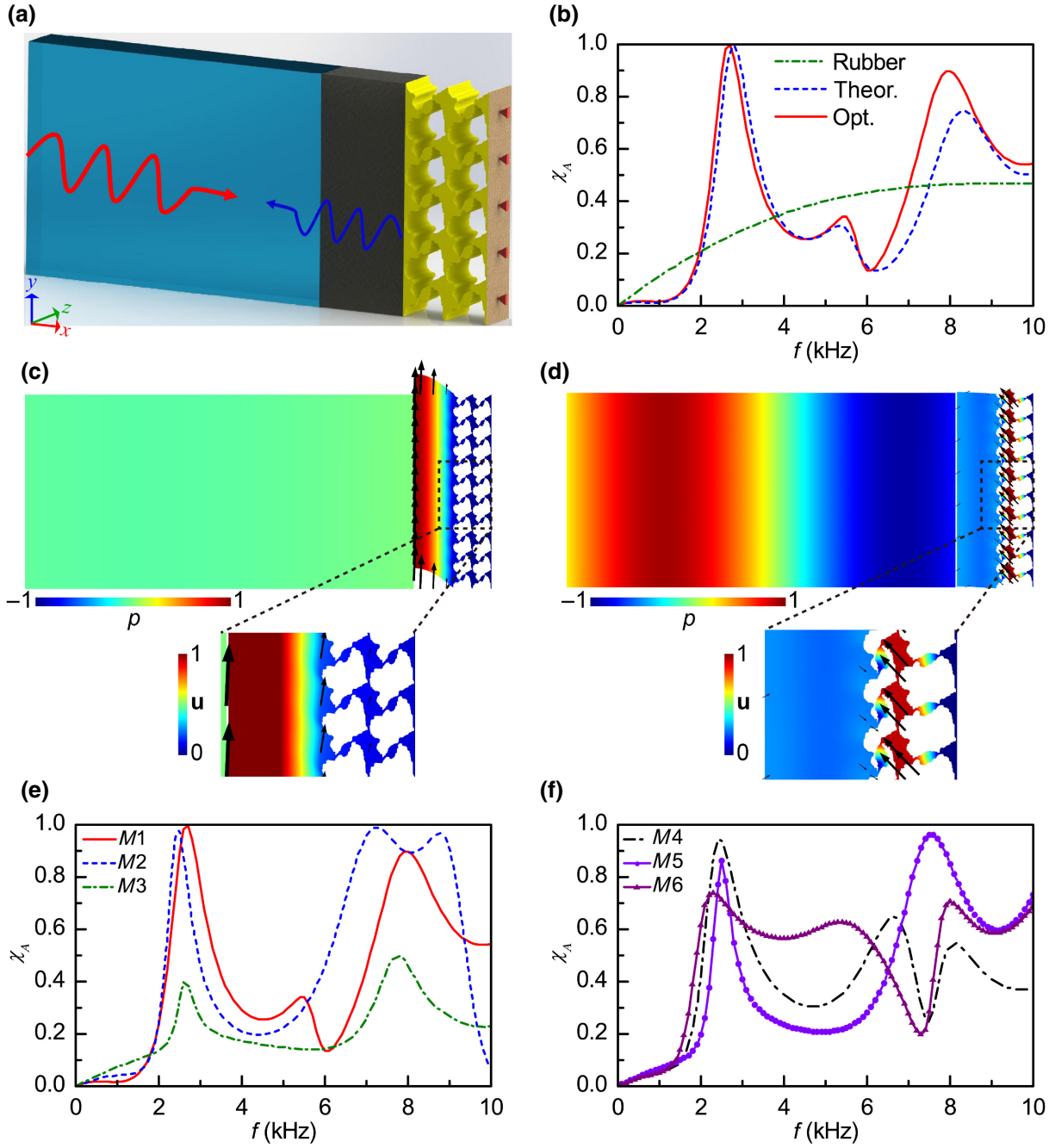

FIG. 14. Underwater sound absorption using various representative inverse-designed metasurfaces. (a) Schematic model for underwater sound absorption. The L wave is incident from the background water. The rubber layer is attached to the metasurface whose right edge is fixed. (b) The sound absorption spectrum using optimized (Opt.) metasurface $M1$ and theoretical (Theor.) absorption for $(C_{11},\ C_{66},\ C_{16}) = (C_{11}^0,\ C_{11}^0,\ 0.98C_{11}^0)$. (c) and (d) Acoustic pressure (p) and displacement fields (u) in the background water, rubber layer, and metasurface for the maximal (c) and minimal (d) absorptions at 2700 and 6100 Hz shown in (b). (e) and (f) Comparisons of the absorption curves among metasurfaces $M1$–$M3$ (e) and $M4$–$M6$ (f). The thickness and viscoelastic isotropic loss ξ of the rubber layer are set as 2 cm and 0.2, respectively.

the thickness and the loss factor of the rubber. Detailed discussions are provided in the following paragraphs.

As shown in Fig. 14(c), the rubber layer shows an obvious transverse wave mode, thus completely neutralizing or annulling the reflected acoustic wave in the water. Conversely, in Fig. 14(d) associated with a low absorption at 6.1 kHz, the wave field shows that the motion of the rubber layer is dominated by the longitudinal wave mode, which causes a distinct longitudinal wave reflection into water, responsible for the low absorption.

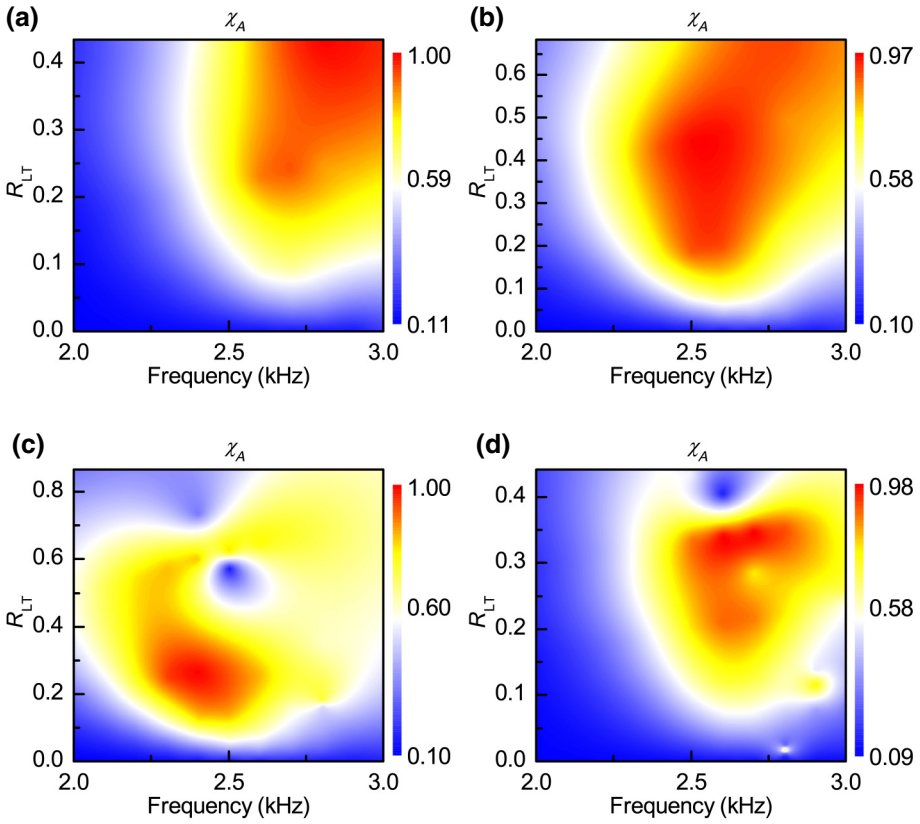

FIG. 15. Relation between reflective conversion R_{LT} of a theoretical anisotropic elastic homogeneous medium and underwater sound absorptions. (a) Varying C_{16} from $0.01C_{11}^0$ to $0.99C_{11}^0$ for $(C_{11},\ C_{66}) = (C_{11}^0,\ C_{11}^0)$. (b) Varying C_{16} from $0.01C_{11}^0$ to $0.707C_{11}^0$ for $(C_{11},\ C_{66}) = (C_{11}^0,\ 0.5C_{11}^0)$. (c) Varying C_{16} from $0.01C_{11}^0$ to $0.54C_{11}^0$ for $(C_{11},\ C_{66}) = (C_{11}^0,\ 0.3C_{11}^0)$. (d) Varying C_{16} from $0.01C_{11}^0$ to $0.495C_{11}^0$ for $(C_{11},\ C_{66}) = (0.5C_{11}^0,\ 0.5C_{11}^0)$. The reflective L-to-T conversion model and underwater simulation model are based on Figs. 1(b) and 14(a), respectively, for the frequency range 2000–3000 Hz. The thickness of the metasurface layer is 2 cm.

When the reflective transverse wave propagates through the solid medium composed of rubber and metasurface layers, the classic FP resonance condition $kd = N\pi$ yields a generalized FP resonance frequency f_{FP}. The transverse wave velocity of the effective solid medium (rubber-metasurface) can be retrieved by

$$c_{\text{eff}} = \sqrt{\frac{\left(\frac{1}{C_{66\text{ - rubber}}} + \frac{1}{C_{66\text{ - meta}}}\right)^{-1}}{\rho_{\text{eff}}}}. \tag{60}$$

Without consideration of the loss of the rubber, f_{FP} can be determined by

$$f_{FP} = \frac{N\sqrt{\frac{\left(\frac{1}{C_{66,\text{rubber}}} + \frac{1}{C_{66,\text{meta}}}\right)^{-1}}{\rho_{\text{eff}}}}}{2d}, \tag{61}$$

where ρ_{eff} is the effective mass density; N is an integer; d is the thickness of the medium; and $C_{66,\text{rubber}}$ and $C_{66,\text{meta}}$ are the shear moduli of the rubber and the metasurface, respectively.

Although the metasurface $M1$ only generates a 45% L-to-T wave conversion at 2700 Hz in Fig. 11(c), it can still lead to perfect underwater absorption. The first-order theoretical f_{FP} for the model $M1$ is 2752.88 Hz, which is very close to 2700 Hz. This implies that the total absorption at 2700 Hz is caused by the generalized FP resonance of the double solid layers (rubber and metasurface), which enhances the wave attenuation inside the rubber. Similarly, the generalized FP resonance leads to the first absorption peaks in Figs. 14(e) and 14(f) for the other five metasurfaces ($M2$–$M6$). However, benefiting from the high conversion ratio displayed in Fig. 11, $M1$, $M2$, $M5$, and $M6$ possess second absorption peaks generated by the reflective mode-conversion FP resonances. The two kinds of FP resonance frequencies are far from each other for $M2$, but close to each other for $M6$. To be more specific, the first-order f_{FP} is 1795.42 Hz, but the first-order f_{LT} is 4806.78 HZ. This suggests that this combined FP resonance effect can entail broadband high-efficiency underwater sound absorption.

To clarify the effect of the wave conversion on underwater sound absorption, Fig. 15 presents the variation of

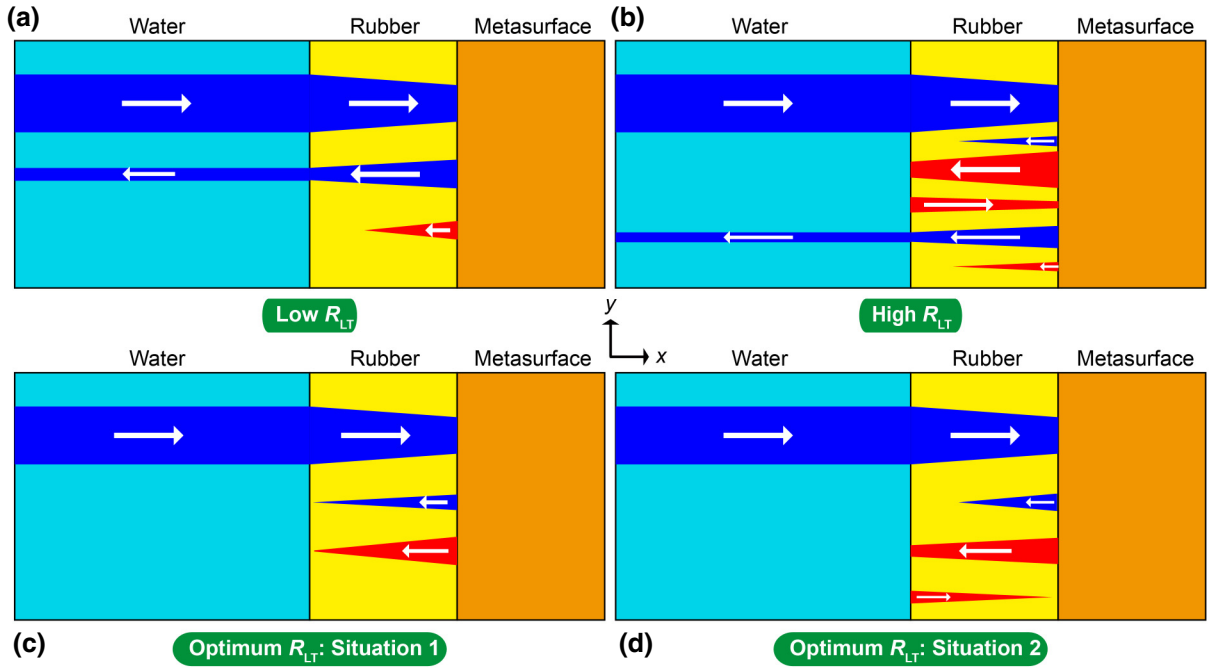

FIG. 16. Schematic of wave propagation and dissipation through the whole model. The arrows signify the direction of wave propagation. Blue and red shapes represent the L and T waves, respectively. The width of the red or blue regions indicates the wave amplitude. The width variation means amplitude decay of the wave. (a) Low RLT; (b) High RLT; (c) Optimum RLT; (d) Another optimum RLT.

R_{LT} of anisotropic solids with the frequency and χ_A under different parameter combinations. As shown in Fig. 15(a), for the same R_{LT}, a higher frequency usually has a higher absorption. However, it can be observed that some cases of high frequency are worse than that of low frequency, such as $R_{LT} = 0.22$. For the same frequency within the range 2500–3000 Hz, a higher R_{LT} gives rise to a higher absorption. When R_{LT} only takes about 40% instead of 100%, total absorption is realized by the metasurface and rubber layer. The comparison between Figs. 15(a) and 15(b) indicates that the operating frequency corresponding to nearly 100% absorption decreases when C_{66} becomes smaller. Around 2500 Hz, the highest absorption occurs in the R_{LT} range of 0.3 to 0.4. It is worth noting that a larger red zone means that the same parameter combination can realize a high absorption of a certain bandwidth. When C_{66} further decreases, Fig. 15(c) shows that a lower R_{LT} can lead to 100% absorption. Meanwhile, Fig. 15(c) also indicates

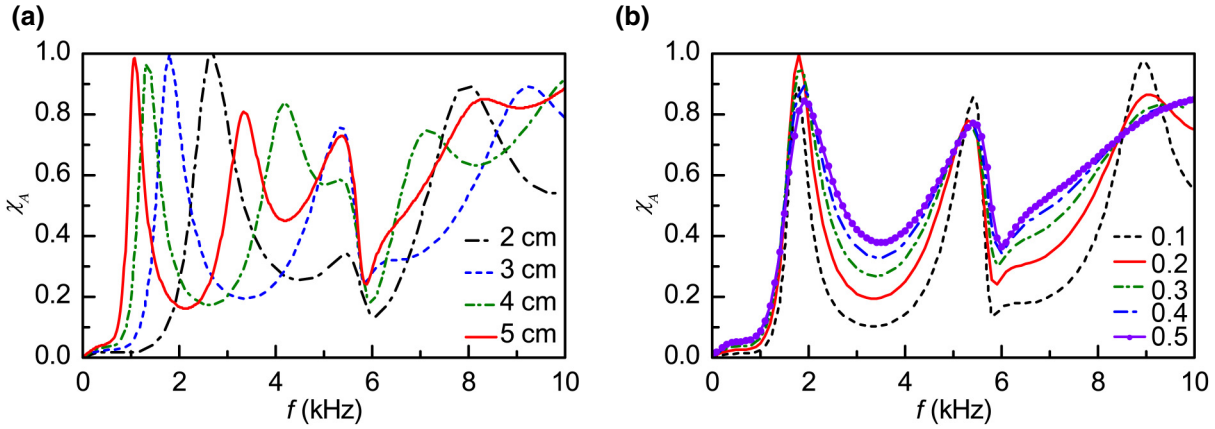

FIG. 17. Effects of the rubber layer on the underwater absorption using $M1$. (a) Effect of the thickness of the rubber layer varying from 2 to 5 cm when the viscoelastic isotropic loss is 0.2. (b) Effect of the viscoelastic isotropic loss ξ of the rubber layer ranging from 0.1 to 0.5 when the thickness of the rubber layer is 3 cm.

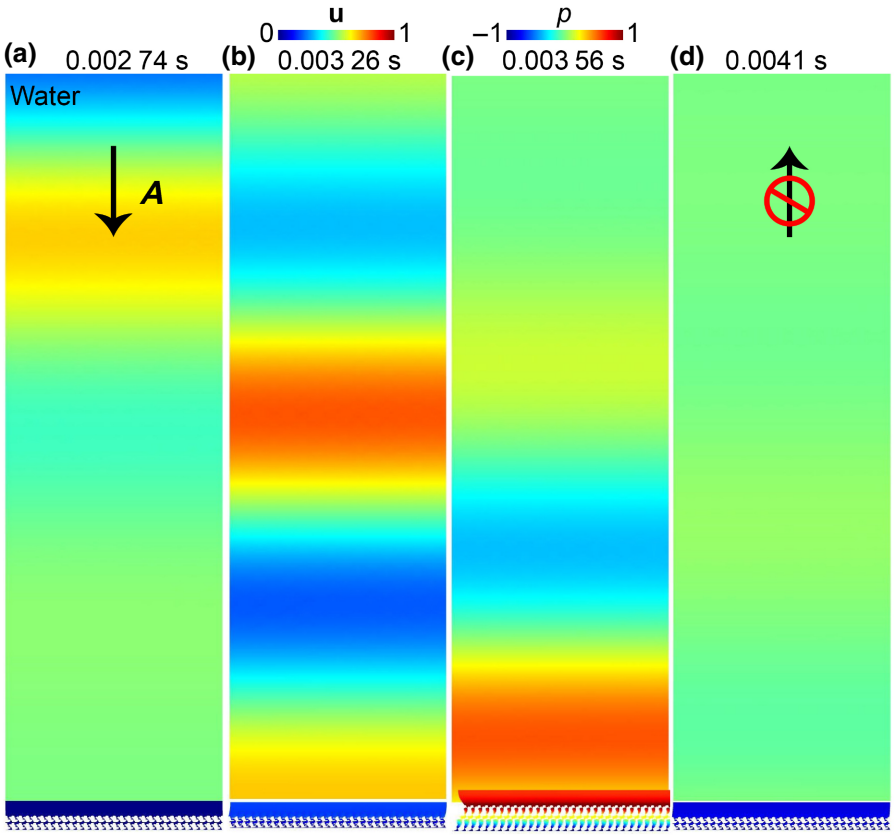

FIG. 18. (a)–(d) Time-domain response of near-perfect underwater sound absorption based on $M1$. An acoustic wave is incident from the water and then causes the mode conversion and absorption. The symbol A represents the incident acoustic wave. The thickness and viscoelastic isotropic loss of the rubber layer are selected as 2 cm and 0.2. respectively.

that a higher R_{LT} cannot guarantee a higher absorption under the specific parameter combinations. Compared with Fig. 15(a), Fig. 15(d) demonstrates that the nearly 100% absorption only requires a low R_{LT} when both C_{11} and C_{66} decrease simultaneously.

To sum up, there is no monotonic correlation between the wave conversion and underwater sound absorption. Firstly, achieving 100% absorption requires a proper conversion. Secondly, for different parameter combinations, it is always possible to find the proper conversion to achieve 100% absorption. Thirdly, a lower C_{66} would favor 100% absorption at a lower frequency. Fourthly, most quasitotal absorption occurs when the conversion is smaller than 0.5. To a certain extent, Fig. 15 also shows the possibility for broadband high absorption.

To better reveal the discovered mode-conversion mechanism, Fig. 16 displays the complete process including the L wave in the solids caused by the incident L wave from water, propagation of T wave, and the mutual conversion between L and T waves. In principle, there are four typical wave propagation scenarios depending on the level of the mode conversion, as shown in Fig. 16. They are summarized as follows.

(i) If the conversion ratio R_{LT} is low, the incident L wave is dissipated to some extent as illustrated in Fig. 16(a). At the interface between the rubber and the metasurface, mode conversion generates the reflected L and T waves. The L wave dominates the reflective wave energy before being further dissipated by the rubber. However, the T wave can be exhausted by the rubber because of the large dissipation of the T waves. The whole process results in partial sound reflection.

(ii) If the conversion ratio R_{LT} is high, as shown in Fig. 16(b), the incident L wave is converted into reflected L and T waves. Because of the high mode conversion efficiency, the latter dominates the reflected wave energy, while the rubber consumes part of reflected T wave energy. The remaining T wave is dissipated by the rubber again, alongside reflected L and T waves at the interface. Again, the reflected T wave can be exhausted by the rubber. Meanwhile, the reflected L wave is dissipated by the rubber again and then propagates into the water. As a result, the absorption does not attain 100% due to the partial reflection in the system.

(iii) If an optimum or "suitable" R_{LT} (called Situation 1) is reached, as shown in Fig. 16(c), the amplitude of the T wave is larger than that of the L wave. With

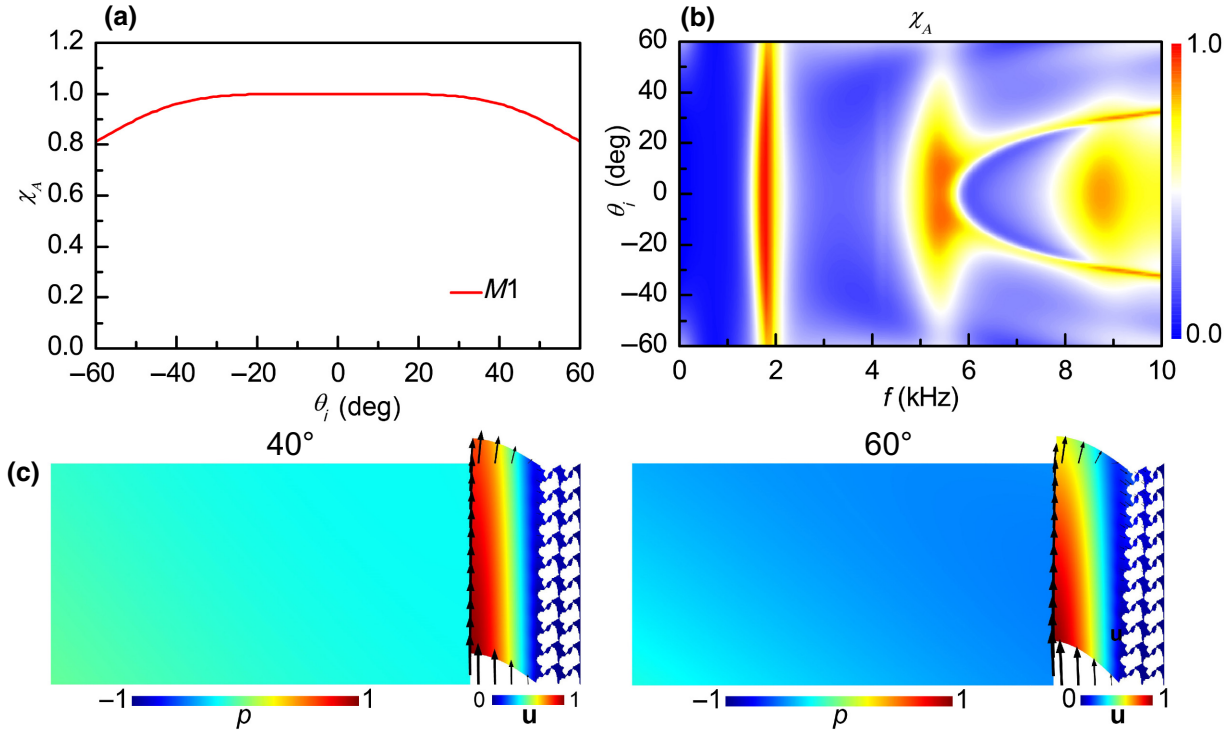

FIG. 19. Effect of the wave incidence angle on the underwater sound absorption using $M1$. (a) Variation of the absorption curve with the wave incidence angle θ_i at 1800 Hz. (b) Absorption contours with the operating frequency changing from 0.5 Hz to 10 kHz and the incidence angle varying from −60° to 60°. (c) Displacement (u) and acoustic (p) pressure fields for the incidence angles of 40° and 60° in (a), respectively. The thickness and viscoelastic isotropic loss of the rubber layer are set as 3 cm and 0.2, respectively.

suitable amplitudes, the two kinds of waves are exactly exhausted by the rubber based on the generalized FP resonance of both layers (rubber and metasurface), which enhances the wave attenuation inside the rubber, realizing total underwater sound absorption.

(iv) If another optimum or suitable R_{LT} (called Situation 2) is reached, as illustrated in Fig. 16(d), the incident L wave still generates reflected L and T waves. While the L wave can be rapidly exhausted by the rubber, only part of the T wave can be dissipated by the rubber. The remaining part of the T wave is reflected by the rubber again. Finally, this secondary reflected T wave is exhausted by the rubber. At this point, perfect sound absorption is generated by the system.

Obviously the so-called suitable reflected L-to-T and T-to-L mode conversion can lead to a high and even 100% underwater sound absorption. In particular, multiple

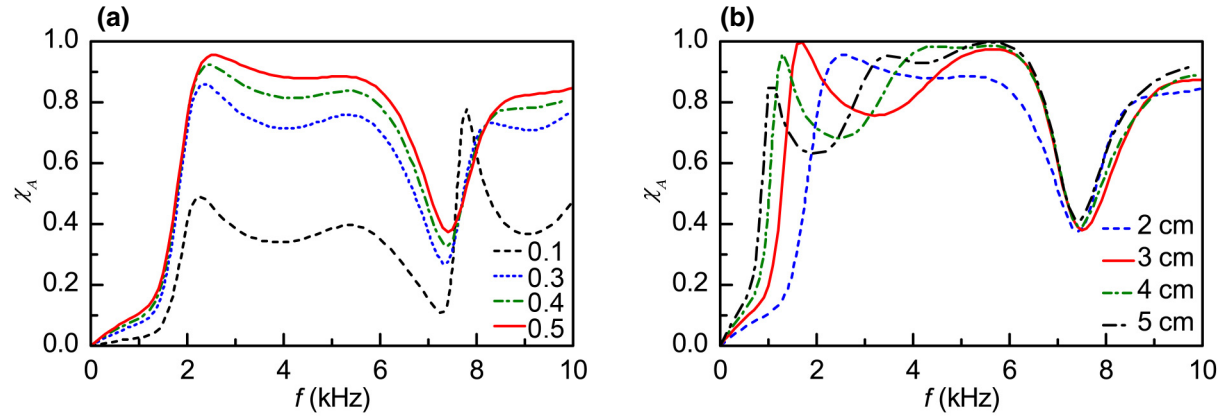

FIG. 20. Effect of the rubber layer on the underwater absorption using $M6$. (a) Effect of the viscoelastic isotropic loss ξ of the rubber layer ranging from 0.1 to 0.5 when the thickness of rubber layer is 2 cm. (b) Effect of the thickness of the rubber layer varying from 2 cm to 5 cm when the viscoelastic isotropic loss is 0.5.

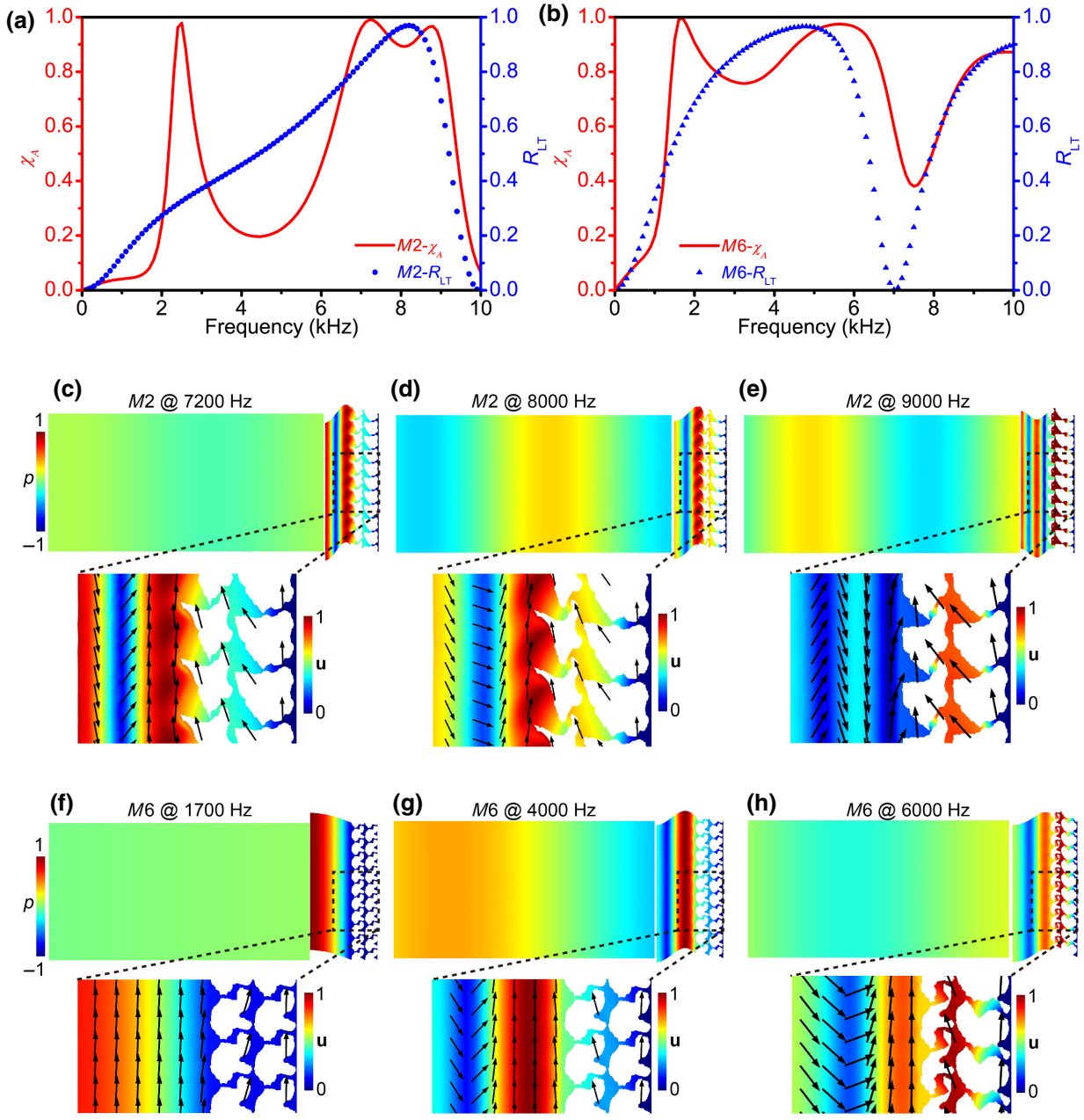

FIG. 21. Broadband sound absorptions and responses of representative metasurfaces. (a) and (b) Relation between absorption and conversion ratio R_{LT} with frequency for $M2$ in Fig. 14(e) and $M6$ in Fig. 20(b). (c)–(h) Acoustic (p) and elastic (u) fields for $M2$, (c)–(e), and $M6$, (f)–(h). The thickness and viscoelastic isotropic loss ξ of the rubber layer are 2 cm and 0.2 for $M2$, and 3 cm and 0.5 for $M6$.

conversions occur when the reflective conversion ratio is high. Therefore, our proposed rubber-metasurface bilayer can support different levels of mode conversion, and multiple reflections and conversions simultaneously.

In fact, the absorption performance of the whole coating is affected by the rubber layer. To quantitatively show the role of the rubber layer, Figs. 17(a) and 17(b) illustrate the effect of the thickness and the viscoelastic isotropic loss ξ of the rubber layer on absorption. With increasing thickness, the frequency of the first absorption peak gradually decreases while keeping the ultrahigh absorption efficiency. In particular, the coating delivers 98.6% absorption at 1080 Hz with a 5-cm-thick rubber layer. However, the effect of the viscoelastic loss is nonmonotonic, i.e., 0.2 and 0.5 lead to the highest and lowest absorption, respectively. Therefore, choosing suitable viscoelastic loss of the rubber layer is very important. In all cases, it is the effective L-to-T wave conversion that allows underwater low-frequency perfect absorption.

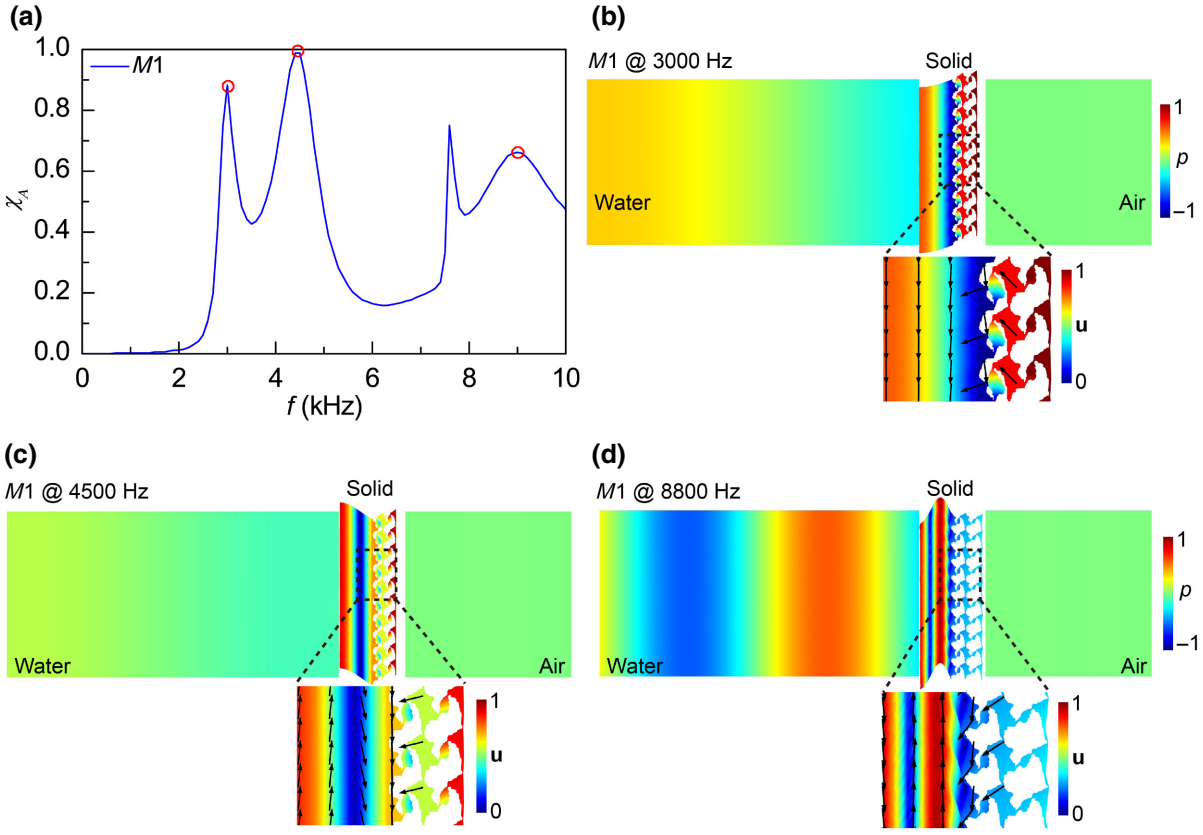

FIG. 22. Sound absorption of a water-solid-air model using $M1$. (a) Absorption curve for the model where steel backing is replaced by the air region considering the air-structure interaction. (b)–(d) Acoustic (p) and elastic (u) fields at representative frequencies marked in (a).

To reveal the underwater near-perfect absorption, Fig. 18 shows the time-domain response of the whole model with the rubber layer and metasurface under the incident acoustic wave at 2700 Hz [26]. Figures 18(a)–18(c) show that the incident acoustic wave causes the apparent resonance of the metasurface and the transverse motion of the rubber layer. The significant dissipation of the transverse energy in the rubber layer leads to near-perfect underwater sound absorption, i.e., no obvious reflected acoustic wave is excited by the rubber layer and metasurface.

This study mainly focuses on normal incidence cases. To check the sensitivity of the optimized metasurface to cope with an angle of incidence, Fig. 19(a) shows the absorption result at 1800 Hz when the incident angle of the acoustic wave varies from $-60°$ to $60°$. Remarkably, the metasurface can still induce quite a high absorption, typically exceeding 80%, within the considered incidence angle range. Figure 19(b) shows that the metasurface can realize 50%–80% absorption at 5300 and 9300 Hz within the whole incidence angle range. From the acoustic pressure and displacement fields in Figs. 19(c) and 19(d), the rubber layer shows an obvious T wave mode even though the incident wave impinges from an oblique direction. Although this study only considers normal incidence, the coating based on the metasurface still has a high absorption performance within a wide range of incidence angles. This directly demonstrates the robustness of the anisotropic metasurfaces and reflective L-to-T wave conversion.

In view of the broadband feature of $M6$ shown in Fig. 11(c) and the obvious effect of the rubber layer, Figs. 20(a) and 20(b) present the variations of the absorption of $M6$ with the viscoelastic loss and the thickness of the rubber layer. With an increase of loss, the whole broadband absorption efficiency gradually increases. With the specific $\xi = 0.5$, a broadband absorption higher than 80% is obtained within the range of 2000 to 6000 Hz. For $\xi = 0.5$, the effect of the thickness on the absorption is nonmonotonic. The coating can realize a complete (100%) absorption at 1.7 kHz in the case of 3-cm thickness. Meanwhile, high-efficiency ultrabroadband absorption can be generated within 1700–6700 Hz. In short, with the properly selected parameters of the rubber layer, the inverse-designed metasurface is suitable for generating ultrabroadband low-frequency high-efficiency absorption, and is not just limited to the low-frequency perfect

absorption caused by the reflective L-to-T wave conversion. Therefore, this characteristic demonstrates that the reflective L-to-T wave conversion offers a route for engineering an elastic metamaterial design in order to achieve low-frequency and broadband high-efficiency underwater sound absorption.

To explain the broadband sound absorption effect, Fig. 21 presents the absorption curve, conversion ratio, and response fields of the representative metasurfaces $M2$ and $M6$. It is observed from Figs. 21(a) and 21(b) that the broadband absorption appears when the conversion ratio R_{LT} is generally larger than 80% within a broadband range. As displayed in Fig. 21(a), the high R_{LT} is far from the FP resonance frequency. However, a broader range of high-efficiency absorption is generated when the high R_{LT} in Fig. 21(b) is close to the first generalized FP resonance frequency around 2000 Hz. The acoustic and elastic fields in Figs. 21(c)–21(e) show that the polarization angles for $M2$ at the three frequencies slightly change, meaning that the eigenstate carrying L-to-T conversion is relatively stable. The absorption of $M6$ reaches 100% at 1700 Hz, whose polarization is different from those at 4000 Hz and 6000 Hz. At the macroscopic level, it is the asymmetrical solid blocks that create the plagiotropic resonance to induce the transverse motions of the adjacent rubber layer.

Therefore, the metasurface supporting the broadband high-efficiency sound absorption has to possess: (a) a stable slanting polarization; and (b) a proximity effect between the high-efficiency ($>80\%$) conversion ratio and the generalized FP resonance frequency.

In view of the wave-conversion characteristics of elastic metasurfaces, it is possible to replace the steel backing at the right of the model in Fig. 1 with air. As shown in Fig. 22(a), the metasurface $M1$ can still induce very high absorption at 3000 and 4500 Hz. The field maps in Figs. 22(b) and 22(c) show that the plagiotropic polarization of the metasurface causes different levels of transverse motion, thus leading to high-efficiency absorption. When the polarization angle distinctly changes, the absorption effect is weakened accordingly, as depicted in Fig. 22(d). The high underwater sound absorption in Fig. 22 indicates the robustness of wave conversion in both water-solid and water-solid-air models for high-efficiency underwater sound absorption delivered by the anisotropic elastic metasurface. Moreover, the effective elastic wave manipulation by a highly anisotropic solid implies the possibilities of designing a metasurface with high-efficiency wave transmission across two totally different media in the future. Of course, the ideal broadband sound isolation can be achieved by the inverse-designed metasurface as well.

V. CONCLUSIONS

Unlike the transmission-type elastic mode conversion, we present a theoretical scattering framework and an inverse-design approach for reflective metasurfaces that enable L-to-T and T-to-L conversion for energy trapping and dissipation. Benefiting from strong anisotropy and mode coupling, reflective metasurfaces with specific effective parameters can entail different levels of customized multiple mode conversion within subwavelength ranges. We systematically investigate the effects of key effective parameters on the L and T wave reflection coefficients as well as the polarization angles of the wave modes. Moreover, the condition for the reflective mode-conversion FP resonance is analytically given. In addition, the theory can predict the reflective FP resonance frequency for arbitrarily prescribed effective parameter combinations. Subsequently, the inverse-design methodology based on the proposed scattering model and the dynamic effective medium theory is established for the realization of ultrathin anisotropic reflective metasurfaces. Several representative metasurfaces are designed and analyzed to demonstrate the beneficial topological features of an asymmetric block-connection network for arbitrary anisotropy and mode coupling. Finally, some metasurfaces are verified to generate the low-frequency high-efficiency and even broadband high-efficiency underwater sound absorption. In particular, a rubber-metasurface layer in which the metasurface with a thickness of approximately $\lambda/70$ can produce nearly 100% absorption at around 1080 Hz. Even though the inverse design is based on normal wave incidence, the optimized metasurface can still deliver quite a high absorption of over 80% for a wide range of incidence angles ($-60°$ to $60°$). More specifically, the proposed metasurfaces with reflective mode conversion can produce ultrabroadband high-efficiency absorption with an efficiency higher than 75% in the frequency range 1700–6700 Hz, corresponding to a relative bandwidth of 119%. The present reflective mode conversion theory, the inverse-design methodology, and the realization of anisotropic elastic metasurfaces might trigger many potential applications in the fields of vibration isolation, elastic energy absorbers, and nondestructive testing, etc. Meanwhile, the underwater broadband sound absorption mechanism based on the combined reflective FP resonances of the rubber-metasurface layer can offer impetus to underwater cloaking.

In future work, multifunctional reflective metasurfaces considering more engineering constraints and applications should be investigated. In pursuit of broadband and even ultrabroadband features, it is necessary to perform a systematic inverse design of this class of reflective metasurfaces. Consideration of oblique wave incidence and even all-angle features would be an important step forward. Furthermore, combining the present theory with machine learning might allow the realization of three-dimensional large-scale design of elastic metasurfaces for more advanced wave properties and functionalities.

ACKNOWLEDGMENTS

This work was supported by the National Natural Science Foundation of China (Grants No. 12172044, No. 11802012, No. 11972246, No. 12021002, No. 11991031, and No. 11902171), the Beijing Institute of Technology Research Fund Program for Young Scholars, the Hong Kong Scholars Program (Grant No. XJ2018041), the Sino-German Joint Research Program (Grant No. 1355) and the German Research Foundation (DFG, Project No. ZH 15/27–1). H.W.D. would like to thank Professor Yun Jing (Penn State University, U.S.), Dr. Bin Wu (National University of Ireland, Galway, Ireland), Dr. Li Ma (Beijing Institute of Technology, China), Mr. Wenxiao Fu, and Mr. Yuqi Xu (Tianjin University, China) for their helpful discussions.

H.W.D. contributed to conceptualization, methodology, formal analysis, visualization, validation, and writing of the original draft. S.D.Z. contributed to methodology, formal analysis, data curation, and validation. M.O. contributed to conceptualization, methodology, formal analysis, supervision, and review and editing of the paper. C.S. contributed to methodology, formal analysis, and discussion. C.Z. contributed to discussion and review and editing of the paper. L.C., Y.S.W., and D.F. were involved in supervision, reviewing and editing the paper, and project administration.

The authors declare that they have no known competing financial interests or personal relationships that could have appeared to influence the work reported in this paper.

APPENDIX A: DERIVATION OF THE AMPLITUDE OF S_{LT} USING REFLECTIVE SOLID-SOLID MODEL

Specific expressions during the derivation of the expression of the amplitude of the scattering components can be written as

$$W_1 = 2k_L C_{11}^0[-P_y(C_{16}Q_x + C_{66}Q_y)\beta\cos(\beta d)\sin(\alpha d) + (C_{16}P_x + C_{66}P_y)Q_y\alpha\cos(\alpha d)\sin(\beta d)], \quad \text{(A1)}$$

$$W_2 = [k_T C_{66}^0(C_{11}Q_x + C_{16}Q_y) - k_L C_{11}^0 P_x(C_{16}Q_x + C_{66}Q_y)]\beta\cos(\beta d), \quad \text{(A2)}$$

$$W_3 = C_{11}^0 C_{66}^0 k_L k_T(P_y Q_x - P_x Q_y)\sin(\beta d), \quad \text{(A3)}$$

$$W_4 = (C_{16}^2 - C_{11}C_{66})(P_y Q_x - Q_x P_y)\beta\cos(\beta d), \quad \text{(A4)}$$

$$W_5 = C_{11}^0 k_L(C_{16}P_x + C_{66}P_y)Q_x - C_{66}^0 k_T(C_{11}P_x + C_{16}P_y)Q_y\sin(\beta d). \quad \text{(A5)}$$

Therefore, S_{LT} can be defined as

$$S_{LT} = \frac{W_1}{\sin(\alpha d)(W_2 + iW_3) \; + \; \alpha\cos(\alpha d)(W_5 + iW_4)}. \quad \text{(A6)}$$

For the amplitude of S_{LT}, two following expressions can be defined as

$$M_1 = W_5\alpha\cos(\alpha d) + W_2\sin(\alpha d), \quad \text{(A7)}$$

$$M_2 = W_4\alpha\cos(\alpha d) + W_3\sin(\alpha d). \quad \text{(A8)}$$

So, Eq. (A6) can be further rewritten as

$$S_{LT} = \frac{W_1}{M_1 + iM_2}. \quad \text{(A9)}$$

Accordingly, the amplitude of S_{LT} can be expressed by

$$|S_{LT}| = \sqrt{\left(\frac{W_1 M_1}{M_1^2 + M_2^2}\right)^2 + \left(\frac{-W_1 M_2}{M_1^2 + M_2^2}\right)^2} = C_{11}^0 k_L \sqrt{\frac{[P_y(C_{16}Q_x + C_{66}Q_y)\beta\sin(\alpha d)\cos(\beta d) - Q_y(C_{16}P_x + C_{66}P_y)\alpha\cos(\alpha d)\sin(\beta d)]^2}{\left\{\begin{array}{l}[(C_{66}^0 k_T P_y(C_{11}Q_x + C_{16}Q_y) - C_{11}^0 k_L P_x(C_{16}Q_x + C_{66}Q_y))\beta\sin(\alpha d)\cos(\beta d) \\ +(C_{11}^0 k_L(C_{16}P_x + C_{66}P_y)Q_x - C_{66}^0 k_T(C_{11}P_x + C_{16}P_y)Q_y)\alpha\cos(\alpha d)\sin(\beta d)]^2 \\ +(P_y Q_x - P_x Q_y)^2[(C_{16}^2 - C_{11}C_{66})\alpha\beta\cos(\alpha d)\cos(\beta d) + C_{11}^0 C_{66}^0 k_L k_T\sin(\alpha d)\sin(\beta d)]^2\end{array}\right\}}}. \quad \text{(A10)}$$

APPENDIX B: DYNAMIC EFFECTIVE MEDIUM THEORY OF ANISOTROPIC ELASTIC METASURFACES

To obtain the effective mass density tensor of the anisotropic metamaterials shown in Fig. 8, the time-harmonic eigenstate field is applied on the microstructural boundary. According to the Newton's second law, the corresponding relationship between the applied field and the reaction force on the boundary can be defined as

$$\begin{bmatrix} F_1^* \\ F_2^* \end{bmatrix} = -\omega^2 V \begin{bmatrix} \rho_{11} & \rho_{12} \\ \rho_{21} & \rho_{22} \end{bmatrix} \begin{bmatrix} U_1^0 \\ U_2^0 \end{bmatrix}, \tag{B1}$$

where $F_1^*(F_2^*)$ is the effective net force exerted on the microstructures along the x (y) direction; V represents the volume of the effective medium; ρ_{ij} $(i, j = 1, 2)$ are the effective mass densities; and U_i^0 is the applied displacement.

To obtain the effective elasticity tensor of the anisotropic metamaterial shown in Fig. 8, the eigenstate field of the global strains is applied to the boundaries of the microstructure by

$$\mathbf{E}^0 = \begin{bmatrix} \varepsilon_{11}^0 & \varepsilon_{12}^0 \\ \varepsilon_{21}^0 & \varepsilon_{22}^0 \end{bmatrix}, \tag{B2}$$

where ε_{ij}^0 $(i, j = 1, 2)$ indicates the prescribed macrostrains of the microstructure.

To derive the effective elastic constants, the energy equivalence between the induced energy on the microstructural boundaries and the strain energy of the effective medium can be described by [8]

$$\sum_{\Gamma} \mathbf{F}^* \cdot \mathbf{u}^* = C_{ijkl} \varepsilon_{ij}^0 \varepsilon_{kl}^0 V, \tag{B3}$$

where $\mathbf{F}^*$ and $\mathbf{u}^*$ are the reaction force vector and applied displacement vector; and Γ denotes the four edges of the microstructures in Fig. 8(b).

The applied eigenstate field is defined by $\mathbf{u} = \mathbf{E}^0 \cdot \mathbf{r} e^{i\omega t}$ where $\mathbf{r} = [x, y]^{\mathrm{T}}$ is the position vector. For the retrieval of C_{11} and C_{21} (C_{12}), the prescribed global strain field is given by

$$\mathbf{E}_{C_{11}}^0 = \begin{bmatrix} 1 & 0 \\ 0 & 0 \end{bmatrix}. \tag{B4}$$

The global strain field for retrieving C_{66X} and C_{26} is given by

$$\mathbf{E}_{C_{66X}}^0 = \begin{bmatrix} 0 & 1 \\ 0 & 0 \end{bmatrix}. \tag{B5}$$

The global strain field for retrieving C_{66Y} and C_{16} is given by

$$\mathbf{E}_{C_{66Y}}^0 = \begin{bmatrix} 0 & 0 \\ 1 & 0 \end{bmatrix}. \tag{B6}$$

In the framework of the dynamic effective medium theory, the equations of motion of anisotropic elastic solids can be written as

$$C_{ijkl} u_{l,jk} = \rho_{ij} \ddot{u}_j, \ (i, j, k, l = x, y, z) \tag{B7}$$

where ρ_{ij} denotes the effective mass density tensor in Eq. (B1).

The displacement field of a plane time-harmonic bulk wave can be expressed as

$$u_i = U_i e^{ik(n_j x_j - v)}, \tag{B8}$$

By substituting Eq. (B8) into Eq. (B7), the Christoffel's equation can be obtained as

$$(C_{ijkl} n_k n_j - v^2 \rho_{il}) U_l = 0, \tag{B9}$$

Therefore, the phase velocity of the anisotropic metamaterial can be determined by

$$|\Lambda_{il} - v^2 \rho_{il}| = 0, \tag{B10}$$

where the formula $\Lambda_{il} = C_{ijkl}$.

APPENDIX C: ELASTIC METASURFACES WITH OTHER EFFECTIVE PARAMETER COMBINATIONS

In addition to the six representative metasurfaces in Figs. 11, Fig. 23 shows the optimized topologies and the L-to-T conversion efficiency of other three metasurfaces $M7$–$M9$. Compared with $M3$ in Fig. 11, $M7$, $M8$, and $M9$ bear different topologies with two voids. However, the number of voids is smaller than in $M5$ in Fig. 11. This implies that, under the premise of asymmetric solid blocks connected with narrow rods and the same C_{11} and C_{66}, more voids can result in weaker coupling between the longitudinal and transverse waves. Figure 23(b) shows that the R_{LT} of $M9$ is significantly larger than those of $M7$ and $M8$ in the whole frequency range. Metasurface $M7$ possesses a higher conversion efficiency than $M8$, but $M8$ behaves better than $M7$ in the frequency range above 9000 Hz. This indicates that, under the same conditions as C_{11}, the smaller difference between C_{66} and C_{16} usually leads to a higher reflective conversion efficiency. Very small C_{16} only contributes to the wave conversion at high frequencies.

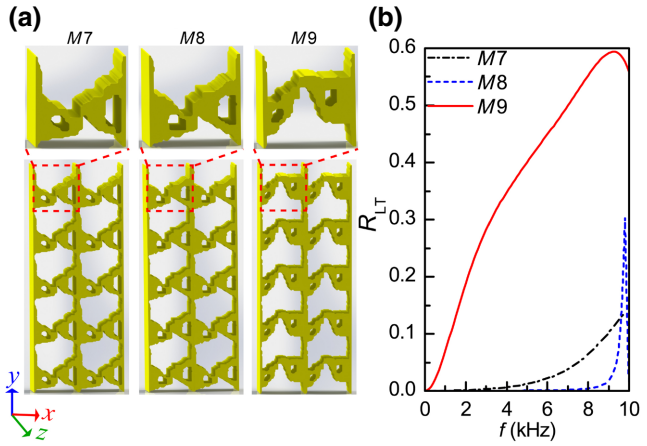

FIG. 23. Topologies and wave reflection coefficients of supplementary metasurfaces. (a) Topologies for different targeted effective parameter combinations. (b) Normalized wave reflection R_{LT} with frequency of different metasurfaces. The targeted parameter combinations are $M7$, $(C_{11},\ C_{66},\ C_{16}) = (C_{11}^0,\ C_{11}^0,\ 0.3C_{11}^0)$; $M8$, $(C_{11},\ C_{66},\ C_{16}) = (C_{11}^0,\ C_{11}^0,\ 0.1C_{11}^0)$; and $M9$, $(C_{11},\ C_{66},\ C_{16}) = (C_{11}^0,\ 0.7C_{11}^0,\ 0.5C_{11}^0)$, respectively.

[1] Z. Liu, X. Zhang, Y. Mao, Y. Y. Zhu, Z. Yang, C. T. Chan, and P. Sheng, Locally resonant sonic materials, Science **289**, 1734 (2000).

[2] M. Oudich, Y. Li, B. M. Assouar, and Z. Hou, A sonic band gap based on the locally resonant phononic plates with stubs, New J. Phys. **12**, 083049 (2010).

[3] Y. Wu, Y. Lai, and Z. Q. Zhang, Elastic Metamaterials with Simultaneously Negative Effective Shear Modulus and Mass Density, Phys. Rev. Lett. **107**, 105506 (2011).

[4] Y. Lai, Y. Wu, P. Sheng, and Z. Q. Zhang, Hybrid elastic solids, Nat. Mater. **10**, 620 (2011).

[5] P. Wang, F. Casadei, S. Shan, J. C. Weaver, and K. Bertoldi, Harnessing Buckling to Design Tunable Locally Resonant Acoustic Metamaterials, Phys. Rev. Lett. **113**, 014301 (2014).

[6] Y. Chen, G. Hu, and G. Huang, A hybrid elastic metamaterial with negative mass density and tunable bending stiffness, J. Mech. Phys. Solids **105**, 179 (2017).

[7] Y. Chen, X. Li, G. K. Hu, M. R. Haberman, and G. Huang, An active mechanical Willis meta-layer with asymmetric polarizabilities, Nat. Commun. **11**, 3681 (2020).

[8] H. W. Dong, S. D. Zhao, Y. S. Wang, and C. Zhang, Topology optimization of anisotropic broadband double-negative elastic metamaterials, J. Mech. Phys. Solids **105**, 54 (2017).

[9] H. W. Dong, S. D. Zhao, X. B. Miao, C. Shen, X. Zhang, Z. Zhao, C. Zhang, Y. S. Wang, and L. Cheng, Customized broadband pentamode metamaterials by topology optimization, J. Mech. Phys. Solids **152**, 104407 (2021).

[10] R. Zhu, H. Yasuda, G. L. Huang, and J. K. Yang, Kirigami-based elastic metamaterials with anisotropic mass density for subwavelength flexural wave control, Sci. Rep. **8**, 483 (2018).

[11] W. Wang, B. Bonello, B. Djafari-Rouhani, Y. Pennec, and J. Zhao, Double-negative Pillared Elastic Metamaterial, Phys. Rev. Appl. **10**, 064011 (2018).

[12] L. Cao, Y. Zhu, Y. Xu, S. W. Fan, Z. Yang, and B. Assouar, Elastic bound state in the continuum with perfect mode conversion, J. Mech. Phys. Solids **154**, 104502 (2021).

[13] D. J. Colquitt, A. Colombi, R. V. Craster, P. Roux, and S. R. L. Guenneau, Seismic metasurfaces: Sub-wavelength resonators and Rayleigh wave interaction, J. Mech. Phys. Solids **99**, 379 (2017).

[14] A. Colombi, P. Roux, S. Guenneau, P. Gueguen, and R. V. Craster, Forests as a natural seismic metamaterial: Rayleigh wave bandgaps induced by local resonances, Sci. Rep. **6**, 19238 (2016).

[15] R. Zhu, X. N. Liu, G. K. Hu, C. T. Sun, and G. L. Huang, Negative refraction of elastic waves at the deep-subwavelength scale in a single-phase metamaterial, Nat. Commun. **5**, 5510 (2014).

[16] J. M. Kweun, H. J. Lee, J. H. Oh, H. M. Seung, and Y. Y. Kim, Transmodal Fabry-Pérot-Resonance: Theory and Realization with Elastic Metamaterials, Phys. Rev. Lett. **118**, 205901 (2017).

[17] M. S. Kim, W. R. Lee, Y. Y. Kim, and J. H. Oh, Transmodal elastic metasurface for broad angle total mode conversion, Appl. Phys. Lett. **112**, 241905 (2018).

[18] X. Yang, J. M. Kweun, and Y. Y. Kim, Theory for perfect transmodal fabry-perot interferometer, Sci. Rep. **8**, 69 (2018).

[19] S. M. Ivansson, Numerical design of Alberich anechoic coatings with superellipsoidal cavities of mixed sizes, J. Acoust. Soc. Am. **124**, 1974 (2008).

[20] G. S. Sharma, A. Skvortsov, I. MacGillivray, and N. Kessissoglou, Acoustic performance of gratings of cylindrical voids in a soft elastic medium with a steel backing, J. Acoust. Soc. Am. **141**, 4694 (2017).

[21] H. Meng, J. Wen, H. Zhao, and X. Wen, Optimization of locally resonant acoustic metamaterials on underwater sound absorption characteristics, J. Sound Vib. **331**, 4406 (2012).

[22] L. Z. Huang, Y. Xiao, J. H. Wen, H. B. Yang, and X. S. Wen, Analysis of underwater decoupling properties of a locally resonant acoustic metamaterial coating, Chinese Phys. B **25**, 024302 (2016).

[23] B. Yuan, V. F. Humphrey, J. Wen, and X. Wen, On the coupling of resonance and Bragg scattering effects in three-dimensional locally resonant sonic materials, Ultrasonics **53**, 1332 (2013).

[24] H. W. Dong, C. Shen, S. D. Zhao, W. Qiu, H. Zheng, C. Zhang, S. A. Cummer, Y. S. Wang, D. Fang, and L. Cheng, Achromatic metasurfaces by dispersion customization for ultra-broadband acoustic beam engineering, Natl. Sci. Rev. (2022).

[25] H. W. Dong, S. D. Zhao, Y. S. Wang, L. Cheng, and C. Zhang, Robust 2D/3D multi-polar acoustic metamaterials with broadband double negativity, J. Mech. Phys. Solids **137**, 103889 (2020).

[26] See Supplemental Material at http://link.aps.org/supplemental/10.1103/PhysRevApplied.17.044013 for the elastic wave propagation process (Video S1), the enlarged local wave propagation process (Video S2), and the underwater wave propagation process (Video S3) using the metasurface $M1$ at 2700 Hz.